# RIACS

# Performance of Low Dissipative High Order Shock-Capturing Schemes for Shock-Turbulence Interactions

N.D. Sandham and H.C. Yee

# Performance of Low Dissipative High Order Shock-Capturing Schemes for Shock-Turbulence Interactions

N.D. Sandham and H.C. Yee

# Performance of Low Dissipative High Order Shock-Capturing Schemes for Shock-Turbulence Interactions

N. D. Sandham[*]and H. C. Yee[†]

May 15, 1998

## Abstract

Accurate and efficient direct numerical simulation of turbulence in the presence of shock waves represents a significant challenge for numerical methods. The objective of this paper is to evaluate the performance of high order compact and non-compact central spatial differencing employing total variation diminishing (TVD) shock-capturing dissipations as characteristic based filters for two model problems combining shock wave and shear layer phenomena. A vortex pairing model evaluates the ability of the schemes to cope with shear layer instability and eddy shock waves, while a shock wave impingement on a spatially-evolving mixing layer model studies the accuracy of computation of vortices passing through a sequence of shock and expansion waves. A drastic increase in accuracy is observed if a suitable artificial compression formulation is applied to the TVD dissipations. With this modification to the filter step the fourth-order non-compact scheme shows improved results in comparison to second-order methods, while retaining the good shock resolution of the basic TVD scheme. For this characteristic based filter approach, however, the benefits of compact schemes or schemes with higher than fourth order are not sufficient to justify the higher complexity near the boundary and/or the additional computational cost.

[*]Queen Mary and Westfield College, London, UK
[†]NASA Ames Research Center, Moffett Field, CA, USA

1

# 1    Introduction

Time- and space-resolved direct numerical simulation (DNS) of turbulence is feasible for many canonical flow problems (Moin & Mahesh, 1998) and with increased computer power more applied problems such as separation bubbles (Alam & Sandham, 1997) can also be simulated. For many technologically important flows compressibility effects are important. Direct simulation is already playing an important role in understanding effects such as the reduced growth rate of mixing layers as Mach number is increased (Vreman et al., 1996). With high speed compressible flows, however, the potential combination of shock waves and turbulent flow represents a significant challenge for numerical methods. Although standard total variation diminishing (TVD) type of shock-capturing schemes for the Euler equations (Yee, 1989) are now routinely used in high speed blast wave simulations with virtually non-oscillatory, crisp resolution of discontinuities, for the unaveraged unsteady Navier-Stokes equations it was observed (Sandham & Yee 1989) that the clipping behavior near extrema of these schemes led to generally poor accuracy.

In response to this difficulty, subsequent large three-dimensional computations have either operated at low Reynolds and Mach numbers where the shock waves, if present at all, are weak and can be resolved (Luo & Sandham, 1994) or have used hybrid schemes where shock-capturing schemes are turned on only when shock waves are detected (Vreman et al., 1995, Adams & Shariff, 1996, Adams, 1997 and Lee et al., 1997). These calculations have all used base methods of fourth or sixth-order accuracy, well suited to the accurate calculation of turbulence.

Work has continued on model problems to find improved high order shock-capturing schemes. Lumpp (1996a,b) used high order finite volume essentially non-oscillatory (ENO) schemes for vortex pairing test cases and obtained good shock and vortex resolution. However, large grid stencils and high computational cost has prohibited application to three-dimensional problems. Fu and Ma (1997) have developed a scheme where the group velocity near shock waves is fixed by the numerical method such that oscillations near shock waves are sucked into the shock wave itself, giving very sharp shocks. In another development Yee (1997) has developed a class of compact shock-capturing schemes that require smaller grid stencils and operations

count than standard schemes. Gustafsson and Olsson (1995) developed stable higher-order centered schemes with stable numerical boundary condition treatments. For problems containing shocks, Gustafsson and Olsson used a scalar shock-capturing filter. Such schemes have advantages over higher-order ENO schemes which require very large grid stencils even for modest orders of accuracy. (For example, a seven-point grid stencil is required for a second-order ENO scheme.) Yee et al. (1998) proposed a combination of narrow grid stencil of higher-order classical spatial differencing schemes using low order TVD or ENO dissipations as characteristic filters with an artificial compression method (ACM) switch. The ACM switch is the same as Harten (1978) but applied in a slightly different context. The Yee et al. approach is aimed at problems containing vortex convections, shock, shear, vortex and turbulence interactions. These characteristic TVD (and ENO) filters in conjunction with the artificial compression method can even improve fine scale flow structure when applied to existing methods of Yee (1989) and Yee (1997).

A numerical scheme for DNS of shock-turbulence interactions should ideally not be significantly more expensive than the classical fourth or sixth-order compact or non-compact spatial differencing scheme. It should be possible to resolve all scales down to scales of the order of (if necessary) the Kolmogorov scales of turbulence accurately and efficiently, while at the same time being able to capture steep gradients occurring at smaller scales (e.g. a few mean free paths for a strong shock wave). Turbulence mechanisms should not be affected by the numerical scheme resulting directly from the governing equations. Some early direct simulation codes for incompressible flow were unable to sustain turbulence in channel flow due to their properties with respect to aliasing errors. Shock-capturing schemes are dissipative and an important test of their suitability for turbulence is that they are capable of sustaining turbulence. The purpose of the present work is to evaluate a number of candidate schemes discussed in Yee et al. (1998) using model problems. In the first of these, a vortex pairing in a time-developing mixing layer, shock waves form around the vortices. In the second problem, a shock wave impinging on a spatially-evolving mixing layer, the evolving vortices must pass through a shock wave, which in turn is deformed by the vortex passage. From these two-dimensional tests some conclusions can be drawn regarding numerical methods for accurate calculation of vortex motions within an overall shock-

3

capturing framework.

# 2 Numerical Techniques

The numerical methods used for the study are briefly described in this section. The reader is referred to Yee (1989) for a more complete description of the basic shock-capturing approaches and Yee et al. (1998) for the complete scheme.

The classical fourth-order Runge-Kutta time discretization and classical fourth or sixth-order compact or non-compact spatial differencing as **base schemes** are employed. A second-order TVD dissipation is applied as a filter step at the end of the full Runge-Kutta time step in the form of an additional dissipative numerical flux term

$$F^*_{j+\frac{1}{2}} = \frac{1}{2} R_{j+\frac{1}{2}} \Phi_{j+\frac{1}{2}}, \tag{1}$$

where $R$ is the right eigenvector matrix of the flux Jacobian from the Euler equations and $\Phi$ is defined by the TVD shock-capturing scheme. The detailed programming allows the Euler and viscous terms to be computed using separate methods. The basic spatial schemes are (i) non-compact central, (ii) compact central and (iii) predictor-corrector upwind or upwind biased. Non-compact schemes are the standard second, fourth and sixth-order methods. Compact schemes are either the standard symmetric fourth-order or sixth-order Pade schemes (Ciment & Leventhal, 1975, Hirsh, 1975 and Lele, 1992). For the purposes of this paper we concentrate on the central schemes. Comparable accuracy was obtained with the predictor-corrector upwind or upwind biased schemes proposed by Hixon and Turkel (1998).

## 2.1 TVD Dissipation as a Filter Step

The TVD dissipation as a filter step is taken as the diffusive part of an upwind explicit shock-capturing scheme of the Harten-Yee type, described in Yee (1989). (Other comparable schemes are also applicable.) For a second-order upwind TVD scheme the elements of $\Phi_{j+\frac{1}{2}}$, denoted by $\phi^l_{j+\frac{1}{2}}$, are

$$\phi^l_{j+\frac{1}{2}} = \frac{1}{2}\psi(a^l_{j+\frac{1}{2}})(g^l_{j+1} + g^l_j) - \psi(a^l_{j+\frac{1}{2}} + \gamma^l_{j+\frac{1}{2}})\alpha^l_{j+\frac{1}{2}} \tag{2}$$

4

The $\alpha^l_{j+\frac{1}{2}}$ are elements of $R^{-1}_{j+\frac{1}{2}}(Q_{j+1} - Q_j)$, where $Q$ is the vector of conservative variables, and

$$\psi(z) = \sqrt{(\delta + z^2)}, \tag{3}$$

and

$$\gamma^l_{j+\frac{1}{2}} = \frac{1}{2}\frac{\psi(a^l_{j+\frac{1}{2}})(g^l_{j+1} - g^l_j)\alpha^l_{j+\frac{1}{2}}}{\left(\alpha^l_{j+\frac{1}{2}}\right)^2 + \epsilon}. \tag{4}$$

To avoid an additional logical statement in the actual coding, $\epsilon$ is added to the $\gamma^l_j$. The $a^l_{j+\frac{1}{2}}$ are characteristic speeds of the Euler flux evaluated using Roe's average. In all of the computations, we take $\epsilon = 10^{-7}$. We use the flux limiter given by

$$g^l_j = \frac{\alpha^l_{j-\frac{1}{2}}[(\alpha^l_{j+\frac{1}{2}})^2 + \epsilon] + \alpha^l_{j+\frac{1}{2}}[(\alpha^l_{j-\frac{1}{2}})^2 + \epsilon]}{(\alpha^l_{j+\frac{1}{2}})^2 + (\alpha^l_{j-\frac{1}{2}})^2 + 2\epsilon}. \tag{5}$$

Elements of $R_{j+\frac{1}{2}}$ are computed using Roe's averaging procedure. In all of the computations, the value of $\delta$ was taken to be 1/16 to satisfy an entropy condition. The resolution of the fine scale flow structure showed minor sensitivity to the value of this constant. See Yee et al. (1998) for a discussion.

## 2.2 The ACM Switch

An artificial compression modification can be made to the TVD dissipation, hereafter, referred to as "the ACM/TVD filter". The term $\phi^l_{j+1/2}$ is multiplied by a switch designed by Harten (1978)

$$\kappa \max(\theta^l_j, \theta^l_{j+1}), \tag{6}$$

where

$$\theta^l_j = \frac{||\alpha^l_{j+1/2}| - |\alpha^l_{j-1/2}||}{|\alpha^l_{j+1/2}| + |\alpha^l_{j-1/2}| + \epsilon}. \tag{7}$$

This serves to limit the action of the TVD dissipation to the immediate vicinity (within one grid cell) of the discontinuity, as detected by steep gradients in the characteristic variables. The constant $\epsilon = 10^{-7}$ is again used to avoid any potential singularity without an extra logical statement in the actual

5

| Method | Order (Euler) | Order (viscous) | Shock-capturing | Artificial compression | Compact |
|---|---|---|---|---|---|
| CEN44 | 4 | 4 | No | No | No |
| TVD22 | 2 | 2 | Yes | No | No |
| TVD44 | 4 | 4 | Yes | No | No |
| TVD66 | 6 | 6 | Yes | No | No |
| ACM22 | 2 | 2 | Yes | Yes | No |
| ACM44 | 4 | 4 | Yes | Yes | No |
| ACM66 | 6 | 6 | Yes | Yes | No |
| ACM44C | 4 | 4 | Yes | Yes | Yes |
| ACM66C | 6 | 6 | Yes | Yes | Yes |

Table 1: Notation for numerical methods. Order of accuracy refers to the formal order of the base scheme.

coding. The optimum value of $\kappa$ is problem-dependent and will be discussed further in a later section. See Yee et al. (1998) for additional discussion.

The various combinations of schemes that will be used in this paper are shown on Table 1. The notation "TVD" with the various orders attached at the end means the second-order TVD scheme dissipation (without the ACM switch) is used as the filter with the indicated order of the base scheme for the convection and viscous terms. For simplicity of discussion, unless otherwise indicated, the term TVD or ACM scheme means the selected base schemes indicated in Table 1 using the TVD or ACM/TVD filter.

# 3    Test Cases and Reference Solutions

The performance of the candidate schemes is based on a Cartesian grid with an analytical stretching in the y-direction only. For the present study no attempt is made to use a more sophisticated adaptive grid.

## 3.1    Vortex Pairing in a Time-Developing Mixing Layer

The first test case is of vortex growth and pairing in a temporal mixing layer at a convective Mach number equal to 0.8. At this Mach number there are

shock waves (shocklets) that form around the vortices and the problem is to compute accurately the vortex evolution while avoiding oscillations around the shocks. Previous calculations of the problem can be found in Sandham and Reynolds (1989), Lumpp(1996a,b) and Fu and Ma (1997). Here we set up a base flow as in Sandham and Yee (1989)

$$u = 0.5 \tanh(2y), \tag{8}$$

with velocities normalized by the velocity jump $U_1 - U_2$ across the shear layer and distances normalized by vorticity thickness,

$$\delta_\omega = \frac{U_1 - U_2}{(du/dy)_{max}}. \tag{9}$$

Subscripts 1 and 2 refer to the upper $(y > 0)$ and lower $(y < 0)$ streams of fluid respectively. The normalized temperature and hence local sound speed squared is determined from an assumption of constant stagnation enthalpy

$$c^2 = c_1^2 + \frac{\gamma - 1}{2}(U_1^2 - u^2). \tag{10}$$

Equal pressure through the mixing layer is assumed. Therefore, for this configuration of $U_2 = -U_1$ both fluid streams have the same density and temperature for $y \to \pm\infty$. The Reynolds number defined by the velocity jump, vorticity thickness and kinematic viscosity at the free-stream temperature is set here to be 1000. The Prandtl number is set to 0.72, the ratio of specific heats is taken as $\gamma = 1.4$ and Sutherland's law

$$\frac{\mu}{\mu_R} = \frac{(c^2/c_R^2)^{1.5}(1 + 110.3/T_R)}{c^2/c_R^2 + 110.3/T_R} \tag{11}$$

with reference temperature $T_R = 300K$ is used for the viscosity variation with temperature. The reference sound speed squared $c_R^2$ is taken as the average of $c^2$ over the two free streams with $\mu_R$ the viscosity corresponding to $c_R^2$.

Disturbances are added to the velocity components in the form of simple waves. For the normal component of velocity we have the perturbation

$$v' = \sum_{k=1}^{2} a_k \cos(2\pi kx/L_x + \phi_k) \exp(-y^2/b), \tag{12}$$

where $L_x = 30$ is the box length in the $x$−direction and $b = 10$ is the $y$−modulation. In our test case we simulate pairing in the center of the computational box, by choosing the initially most unstable wave $k = 2$ to have amplitude $a_2 = 0.05$ and phase $\phi_2 = -\pi/2$, and the subharmonic wave $k = 1$ with $a_1 = 0.01$ and $\phi_1 = -\pi/2$. The $u$−velocity perturbations are found by assuming that the total perturbation is divergence free. These fluctuations correspond only approximately to eigenfunctions of the linear stability problem for a compressible mixing layer, but they serve the purpose of initiating the instability of the mixing layer and have the advantage as a test case in that they can be easily coded.

Numerically the grid is equally spaced and periodic in the $x$−direction and stretched in the $y$−direction, using the mapping

$$y = \frac{L_y}{2} \frac{\sinh(b_y \eta)}{\sinh(b_y)}, \qquad (13)$$

where we take the box size in the $y$−direction $L_y = 100$, and the stretching factor $b_y = 3.4$. The mapped coordinate $\eta$ is equally spaced and runs from $-1$ to $+1$. The boundaries at $\pm L_y/2$ are taken to be slip walls. For example, at the lower boundary

$$
\begin{aligned}
\rho_1 &= \rho_2, & (14) \\
(\rho u)_1 &= (\rho u)_2, & (15) \\
(\rho v)_1 &= 0, & (16) \\
(E_T)_1 &= [4(E_T)_2 - (E_T)_3]/3, & (17)
\end{aligned}
$$

where subscripts here refer to the grid point and $E_T$ is the total energy.

Sample results for this configuration were obtained from computations on a $201 \times 201$ grid, using the fourth-order non-compact central spatial differencing, and the ACM/TVD filter (ACM44). The constant $\kappa$=0.7 for the $u \pm c$ and $v \pm c$ nonlinear characteristic fields and $\kappa$=0.35 for the $u$ and $v$ linear characteristic fields were used for the computations. Figure 1a shows snapshots of the pressure field at times $t = 40, 80, 120, 160$, illustrating the roll-up of the primary vortices, followed by vortex merging. Figure 1b - 1d show the corresponding density, vorticity and temperature contours. Shock waves form around the vortices, with a peak Mach number ahead of the vortex of approximately 1.55 at $t = 120$. Figure 2 shows the growth of two

measures of shear layer thickness, the vorticity thickness defined by equation (11) and a momentum thickness, defined here by

$$\theta = \int_{-L_y/2}^{L_y/2} \overline{\rho}(U_1 - \overline{u})(\overline{u} - U_2)dy, \qquad (18)$$

with averages being taken over the periodic direction $x$. Both thickness measurements show rapid growth up to a peak at around $t = 120$ followed by decay. The vorticity thickness is generally more sensitive to details of the flow evolution. Because of the finite box in $x$ the flow would eventually relaminarize. This case is used as a reference high resolution case for comparison of schemes in Section 4. It was checked to be adequately converged by running another simulation with $401 \times 401$ grid points.

## 3.2 Shock Wave Impingement on a Spatially-Evolving Mixing Layer

The second test case has been developed to test the behavior of the schemes for shock waves interacting with shear layers where the vortices arising from shear layer instability are forced to pass through a shock wave. An oblique shock is made to impact on a spatially-developing mixing layer at an initial convective Mach number of 0.6. The shear layer vortices pass through the shock system and later through another shock, imposed by reflection from a (slip) wall at the lower boundary. The problem has been arranged so that the Mach number at the outflow boundary is everywhere supersonic, so no explicit outflow boundary conditions are required. This allows us to focus on properties of the numerical schemes rather than on the boundary treatment.

Figure 3 illustrates the nature of the flow on a $321 \times 81$ grid. This result was taken from a laminar flow simulation with no incoming perturbations. The shear layer originates at $x = 0, y = 0$ at the center of the left hand boundary. An oblique shock originates from the top left hand corner and this impacts on the shear layer at around $x = 90$. The shear layer is deflected by the interaction. Afterwards we have a shock wave below the shear layer and an expansion fan above it. The shock wave reflects from the lower solid wall and passes back through the shear layer. The lower wall uses a slip condition so no viscous boundary layer forms and we focus on the shock-wave interaction

| Property | (1) | (2) | (3) | (4) | (5) |
|---|---|---|---|---|---|
| $u-$velocity | 3.0000 | 2.0000 | 2.9709 | 2.9792 | 1.9001 |
| $v-$velocity | 0.0000 | 0.0000 | -0.1367 | -0.1996 | -0.1273 |
| $\theta$ (degrees) | 0.0000 | 0.0000 | 2.6343 | 3.8330 | 3.8330 |
| density $\rho$ | 1.6374 | 0.3626 | 2.1101 | 1.8823 | 0.4173 |
| pressure $p$ | 0.3327 | 0.3327 | 0.4754 | 0.4051 | 0.4051 |
| sound speed $c$ | 0.5333 | 1.1333 | 0.5616 | 0.5489 | 1.1658 |
| Mach number $|M|$ | 5.6250 | 1.7647 | 5.2956 | 5.4396 | 1.6335 |

Table 2: Flow properties for the shock-wave/shear-layer test case in various regions of the flow: (1) upper stream inflow, (2) lower stream inflow, (3) upper stream after oblique shock, (4) upper stream after expansion fan, (5) lower stream after shock wave.

with the unstable shear layer. The full no-slip problem would, however, make a challenging test case for the future.

The inflow is specified again with a hyperbolic tangent profile, this time as

$$u = 2.5 + 0.5\tanh(2y), \tag{19}$$

giving a mixing layer with upper velocity $U_1 = 3$, lower velocity $U_2 = 2$, and hence a velocity ratio of 1.5. Equal pressures and stagnation enthalpies are assumed for the two streams, with convective Mach number, defined by

$$M_c = \frac{U_1 - U_2}{c_1 + c_2}, \tag{20}$$

where $c_1$ and $c_2$ are the free stream sound speeds, equal to 0.6. The reference density is taken as the average of the two free streams and a reference pressure as $(\rho_1 + \rho_2)(U_1 - U_2)^2/2$. This allows one to compute the inflow parameters as given in the first two columns of Table 2. Inflow sound speed squared is found from the relation for constant stagnation enthalpy (12).

The upper boundary condition is taken from the flow properties behind an oblique shock with angle $\beta = 12°$, given in column 3 of Table 2. The table also gives the properties behind the expansion fan (column 4) and after the oblique shock on the lower stream of fluid (column 5) computed by standard

gasdynamics methods with $\beta = 38.118°$. The conditions in regions 4 and 5 do not correspond exactly to the simulations due to the finite thickness of the shear layer in practice. The Mach number of the lower stream after this shock is approximately $M_5 = 1.6335$ and remains supersonic through all the successive shocks and expansion fans up to the outflow boundary. The resulting shock waves are not strong, but tests showed that they could not be computed without using shock-capturing techniques. The lower boundary was specified with the same slip condition used for the pairing case (Equations (16-19)).

The Prandtl number and ratio of specific heats were taken to be the same as for the vortex pairing test case. The Reynolds number was chosen to be 500.

Fluctuations are added to the inflow as

$$v' = \sum_{k=1}^{2} a_k \cos(2\pi k t/T + \phi_k) \exp(-y^2/b), \qquad (21)$$

with period $T = \lambda/U_c$, wavelength $\lambda = 30$, convective velocity $U_c = 2.68$ (defined by $U_c = (U_1 c_2 + U_2 c_1)/(c_1 + c_2)$) and $b = 10$. For $k = 1$ we take $a_1 = 0.05$ and $\phi = 0$, and for $k = 2$ we take $a_2 = 0.05$ and $\phi = \pi/2$. No perturbations are added to the $u-$component of velocity.

The grid is taken to be uniform in $x$ and stretched in $y$ according to equation (15) with $b_y = 1$. This stretching is much milder than for the pairing problem, as we have to resolve the shear layer even when it deflects away from $y = 0$. The box lengths were taken to be $L_x = 200$ and $L_y = 40$.

A reference solution for the pressure, density and temperature fields is shown on figure 4 for a computation on a grid of $641 \times 161$. The computation employs the fourth-order central differencing as the base scheme in conjunction with the ACM/TVD filter (ACM44) with $\kappa = 0.35$ for nonlinear characteristic fields and $\kappa = 0.175$ for the linear characteristic fields. The vortex cores are located by low pressure regions and the stagnation zones between vortices by high pressure regions. The shock waves are seen to be deformed by the passage of the vortices. Another interesting observation is the way the core of the vortex at $x = 148$ has been split into two by its passage through the reflected shock wave. In spite of the relatively high amplitude chosen for the subharmonic inflow perturbation there is no pairing of vortices within the computational box. We do, however, begin to see eddy shock waves around

11

the vortices near the end of the computational box where the local convective Mach number has increased to around 0.66. The oscillations seen near the upper boundary for $x > 120$ occur where the small Mach waves from the initial perturbations arrive at the upper boundary. The use of characteristic boundary conditions should remove this problem. Practically, the amplitude of oscillations is not sufficient to cause numerical instability or affect the remainder of the flow.

# 4    Computational Results

The notation that will be used for discussing the results for different numerical schemes is shown on Table 1. To examine the resolution of the proposed schemes where shock waves are absent, the computation is compared with the CEN44 (the classical spatially fourth-order central differencing for the convection and diffusion terms) before shock waves were developed for the vortex pairing case. Good agreements were obtained.

The performance of these schemes with the presence of shock waves and turbulence is evaluated based on the following factors:

   (a) Effect of the ACM term
   (b) Effect of the order of the base scheme
   (c) Effect of the grid size (grid refinement study)
   (d) Effect of employing a compact or non-compact base scheme
   (e) Effect of the adjustable constant $\kappa$ for the particular physics
   (f) Shear and fine flow structure capturing capability

## 4.1    Vortex Pairing

For an initial comparison of the schemes we compute the test case of Section 3.1 on a grid of $101 \times 101$ with a time step $\Delta t = 0.1$, running up to $t = 160$.

*Effect of the ACM Term*:

Figure 5 shows the effect of the artificial compression method for the vorticity and momentum thickness variation with time for the TVD44 and ACM44 schemes compared with the reference results from a fine grid (Section 3.1). Results from the ACM method are far superior to those from the standard

12

TVD formulation. Note that there is no improvement in the shock resolution since the ACM term limited the amount of dissipation away from high gradient areas whereas the shock resolution is dictated by the flux limiter.

*Effect of the Order of the Base Scheme*:

Figure 6 shows the effect of increasing accuracy from second to fourth and sixth order using the TVD filter (TVD22, TVD44 and TVD66). As can be seen there is almost no improvement as the order of accuracy is raised. Figure 7 shows the same plot for the ACM/TVD filter (ACM22, ACM44 and ACM66). Here there is an improvement, although the results even for the lowest order are quite good. There is little to choose in the shock resolution properties with the variation in order of accuracy. We choose to compare temperature contours, which are most sensitive to oscillations (Lumpp, private communication). Figure 8 shows a comparison of the ACM schemes of various order with the reference solution. All the schemes here capture the shock waves with minimal oscillations. The temperature contours for the TVD filter of the various order using a $101 \times 101$ grid, although not shown, are not even nearly as accurate as the ACM44 using a $41 \times 41$ grid. See the last plot of Figure 15 for a comparison. It can be seen that there is a significant advantage in moving from second to fourth order, but less is gained in moving from fourth to sixth order using TVD or ACM/TVD as a filter. This is in contrast to an isentropic vortex convection test case where there are definite benefits of moving from fourth order to sixth order (Yee et al., 1998). It appears that the effect of order of accuracy are more pronounced for long time integrations of pure convection.

*Effect of the Grid Size (Grid Refinement Study)*:

To investigate the effect of order of the accuracy in more detail we consider simulations on a very coarse grid of $41 \times 41$ points. Such a case corresponds in practice to simulation of scales of turbulence arising from shear layers only two or three computational cells across. Figure 9 shows results for the ACM schemes. To ensure that the fine scale flow structure is fully resolved by the reference grid $201 \times 201$, the same simulation was done on a $401 \times 401$ grid (figures not shown).

13

*Effect of Compact or Non-Compact Base Scheme:*

For wave propagation and computational problems the performance of fourth and sixth-order compact schemes, although more CPU intensive, appears to be superior to their non-compact cousin. For problems with shock waves the benefit of compact over non-compact schemes is less known due to the filter step. Figure 10 shows results for the fourth and sixth-order compact schemes, which are similar to results from the sixth-order non-compact scheme. Again there is little improvement compared with the fourth-order non-compact scheme. A conclusion is that the use of the ACM/TVD in the filter step is essential to get the benefits of moving from second to fourth order, but even with this method there is little benefit in moving to even higher-order schemes.

*Effect of the Adjustable Constant $\kappa$:*

The ACM switch of Harten has been demonstrated to give good shock resolution and to be essential if the benefits of higher-order discretization schemes are to be realized. There is, however, an adjustable parameter $\kappa$ in the formulation, and results are sensitive to the precise choice of its value. Figure 11 illustrates the effect on the result for the pairing test case of reducing the parameter from 0.7 to 0.35. The vorticity and momentum thickness development is improved due to the reduction in numerical dissipation. From the temperature contours on Figure 12 it can be seen that this has been achieved at the cost of formation of small oscillations around the shock wave. For the present problem one would be ready to pay this price to get the more accurate vortex evolution. However, in general it is not known how such numerically-induced oscillations interact with small scales of turbulence. For the current method the correct procedure for a simulation of shock-turbulence interaction would be to find the smallest value of $\kappa$ to resolve the shock waves satisfactorily and then increase the grid resolution until the turbulence is adequately resolved. There are perhaps other formulations of the ACM switch parameter $\kappa$ based on the flow physics that can perform the adjustment to higher values automatically when stronger shock waves are present. This is a subject of future research.

*Shear and Fine Flow Structure Capturing Capability:*

Shock-capturing schemes are designed to accurately capture shock waves, but

with a less accurate capturing capability for contact discontinuities. In fact, the mixing layer seen at a large scale is a contact discontinuity. If one uses enough grid points to resolve the region of high shear in conjunction with physical viscosity, it might not need to be 'captured'. Contact discontinuities relate to the characteristic velocities $u$ and $v$. As an experiment these linear characteristics were computed with no numerical dissipation. Filters were only applied to the nonlinear characteristics fields $u \pm c$ and $v \pm c$ using the ACM44 method. Interestingly, the computation was no less stable than that the full TVD or ACM schemes (applying $\kappa$ to all of the characteristic fields). Figure 13 shows the vorticity thickness evolution and Figure 14 the resulting temperature field. It can be seen that good results were obtained, although there is a trace of oscillation near the shock wave. This could be remedied by increasing $\kappa$ slightly. See Yee et al. (1998) for an illustration. However, the flow features of the shear and fine flow structure are accurately captured with similar resolution as the $201 \times 201$ grid with ACM44 applied to all of the characteristic fields (Figure 15a).

To balance the shear and shock-capturing, one alternative is to switch to a more compressive limiter (see Yee (1989)) for the linear characteristics fields. Another alternative is to reduce the value of $\kappa$ for the $u, v$ linear fields. The comparison of using different values of $\kappa$ for the linear and nonlinear fields is also shown in Figures 13 and 14.

Figure 15 shows the comparison of the different $\kappa$ values for the three grids. Figure 16 shows the comparison of the five classical flux limiters (see Equations (4.34c)-(4.34g) of Yee (1989)) using ACM44.

## 4.2   Shock-Shear Layer Interaction

The test case defined in Section 3.2 was run on a grid of $321 \times 81$ with $\Delta t = 0.12$ up to $t = 120$ with $\kappa = 0.35$. Figure 17 shows the density field for the TVD44 and ACM44 schemes compared with the reference solution ($641 \times 161$ grid). Again it can be seen that the ACM modification is essential for obtaining good vortex evolution (additionally better shock resolution is obtained). For a more quantitative comparison Figures 18 and 19 show slices through the density field between $x = 50$ and $x = 150$ at $y = 0$ (the centerline of the computational domain). From Figure 18 it is apparent that all the standard TVD schemes, of whatever order, miss the correct vortex formation.

15

| Method | Pairing (200 steps) | Shock-wave (100 steps) |
|--------|---------------------|------------------------|
| CEN44  | 19.5                | 22.1                   |
| TVD22  | 18.8                | 22.8                   |
| TVD44  | 23.4                | 26.9                   |
| ACM22  | 19.6                | 23.8                   |
| ACM44  | 24.2                | 27.9                   |

Table 3: CPU times for various numerical options, measured in Cray C90 seconds. For a key to the various methods see Section 4.1.

From Figure 19 there are some visible benefits in moving from second to higher-order differencing, both in the amplitude of the fluctuations and in the correct convective velocity of the vortices. Figures 20 and 21 compare the density contour using limiter 3 and limiter 5. These figures also compare the use of different $\kappa$ values for the linear and nonlinear characteristic fields.

## 4.3 Computational Costs

The research code that we built consists of many schemes and options and thus is far from being an optimum code. Based on this fact, the CPU times for the Cray C90 are given on Table 3 for the two model problems. Times are given in seconds for **200 steps** of the vortex pairing test case on a grid of $101 \times 101$ and for **100 steps** of the shock-wave impingement problem on a grid of $321 \times 81$.

The non-compact base schemes with the ACM/TVD filter are only around 25% more expensive than the same base schemes without ACM/TVD filter. This has been achieved by only requiring one application of the ACM/TVD filter per full time step for the convection terms.

For the Cray C90 it was found that the compact schemes were significantly more expensive, but this result is distorted for the present code by incomplete vectorization. An extra cost of around 2/3 is expected from considerations of operations count.

16

# 5 Conclusions

Two model problems were considered to test the behavior of shock-capturing schemes in flows where the evolution of vortices from shear layer instabilities plays a crucial role. Standard total variation diminishing schemes do not perform well for these problems. It was found that an artificial compression modification gave much improved results and with this approach there are definite benefits in moving from second to fourth-order differencing schemes. The benefits were less pronounced in moving to sixth order. The fourth order ACM44 schemes show highly accurate shock-wave and shear-layer capability. The non-compact fourth-order base scheme requires a five point stencil, the same as the second-order TVD scheme. There is potentially an additional problem near boundaries in that reduced order and/or upwind schemes must be used. Stable boundary conditions such as those proposed by Gustafsson and Olsson (1995) must be applied. If an adaptive grid is used, higher accuracy can be obtained.

**References**

Adams, N.A. 1997 Direct numerical simulation of turbulent supersonic boundary layer flow. *First AFOSR International Conference on DNS and LES*, Ruston, LA, USA.

Adams, N.A. and Shariff, K. 1996 A high-resolution hybrid compact-ENO scheme for shock-turbulence interaction problems. *J. Comput. Phys.* **127**, 27-51.

Alam, M. and Sandham, N.D. 1997b Numerical study of separation bubbles with turbulent reattachment followed by a boundary layer relaxation. *Parallel Computational Fluid Dynamics '97* (Ed. A. Ecer et al.), Elsevier, to appear.

Ciment, M. and Leventhal, H. 1975 Higher order compact implicit schemes for the wave equation, Math. Comp. **29**, 985-994.

Fu, D. and Ma, Y. 1997 A high order accurate difference scheme for complex flow fields. *J. Comput. Phys.* **134**, 1-15. Gustafsson, B. and Olsson, P. 1995 Fourth-order difference methods for hyperbolic IBVPs. *J. Comput. Phys.* **117**, 300-317.

Gustafsson, B. and Olsson, P. 1995 Fourth-order difference methods for hyperbolic IBVPs. *J. Comput. Phys.* **117**, 300-317.

Harten, A. 1978 The Artificial compression method for computation of shocks and contact discontinuities: III Self-adjusting hybrid schemes, *Math. Comp.* **32**, 363-389.

Hirsh, R.S. 1975 Higher order accurate difference solutions of fluid mechanics problems by a compact differencing technique, J. Comput. Phys. **19**, 90-109.

Hixon, R. and Turkel, E. 1998 High-accuracy compact MacCormack-type schemes for computational aeroacoustics. *AIAA paper 98-0365, 36th Aerospace Sciences Meeting & Exhibit*, Jan. 12-15, Reno, NV.

Lele, S. 1992 Compact finite-difference schemes with spectral-like resolution. *J. Comput. Phys.* **86**, 187-210.

Lumpp, T. 1996a A critical review of high-order accurate finite volume ENO-schemes. *First Intl. Symposium on Finite Volumes for Complex Applications*, Rouen, France, July 14-17.

Lumpp, T. 1996b Compressible mixing layer computations with high-order ENO schemes. *15th Intl. Conf. on Num. Meth. in Flui Dynamics*, Monterey, June 1996.

Luo, K.H. and Sandham, N.D. 1994 On the formation of small scales in a compressible mixing layer. In *Direct and Large-Eddy Simulation I*, Kluwer Academic Publishers, 335-346.

Moin, P. and Mahesh, K. 1998 Direct numerical simulation: a tool in turbulence research. *Ann. Rev. Fluid Mech.* **30**, 539-578.

Sandham, N.D. and Reynolds, W.C. 1989 A numerical investigation of the compressible mixing layer. *Report TF-45*, Department of Mechanical Engineering, Stanford University.

Sandham, N.D., and Reynolds, W.C. 1991 Three-dimensional simulations of large eddies in the compressible mixing layer. *J. Fluid Mech.* **224**, 133-158.

Sandham, N.D. and Yee, H.C. 1989 A numerical study of a class of TVD schemes for compressible mixing layers. *NASA Technical Memorandum 102194.*

Vreman, B., Kuerten, H., and Geurts, B. 1995 Shocks in direct numerical simulation of the confined three-dimensional mixing layer. *Phys. Fluids*, to appear.

Vreman, A.W., Sandham, N.D and Luo, K.H. 1996 Compressible mixing layer growth rate and turbulence statistics. *J. Fluid Mech.*, **320**, 235-258.

Yee, H.C. 1989 A class of high-resolution explicit and implicit shock-capturing schemes *NASA Technical Memorandum 101088*

Yee, H. C. 1997 Explicit and implicit multidimensional compact high-resolution shock-capturing methods: Formulation *J. Comput. Phys.* Vol. **131** No. 1, 216-232.

Yee, H. C., Sandham, N. D. and Djomehri, M. J. 1998, Low dissipative high order shock-capturing methods using characteristic based filters. *RIACS Technical Report 98.11, May 1998*, NASA Ames Research Center.
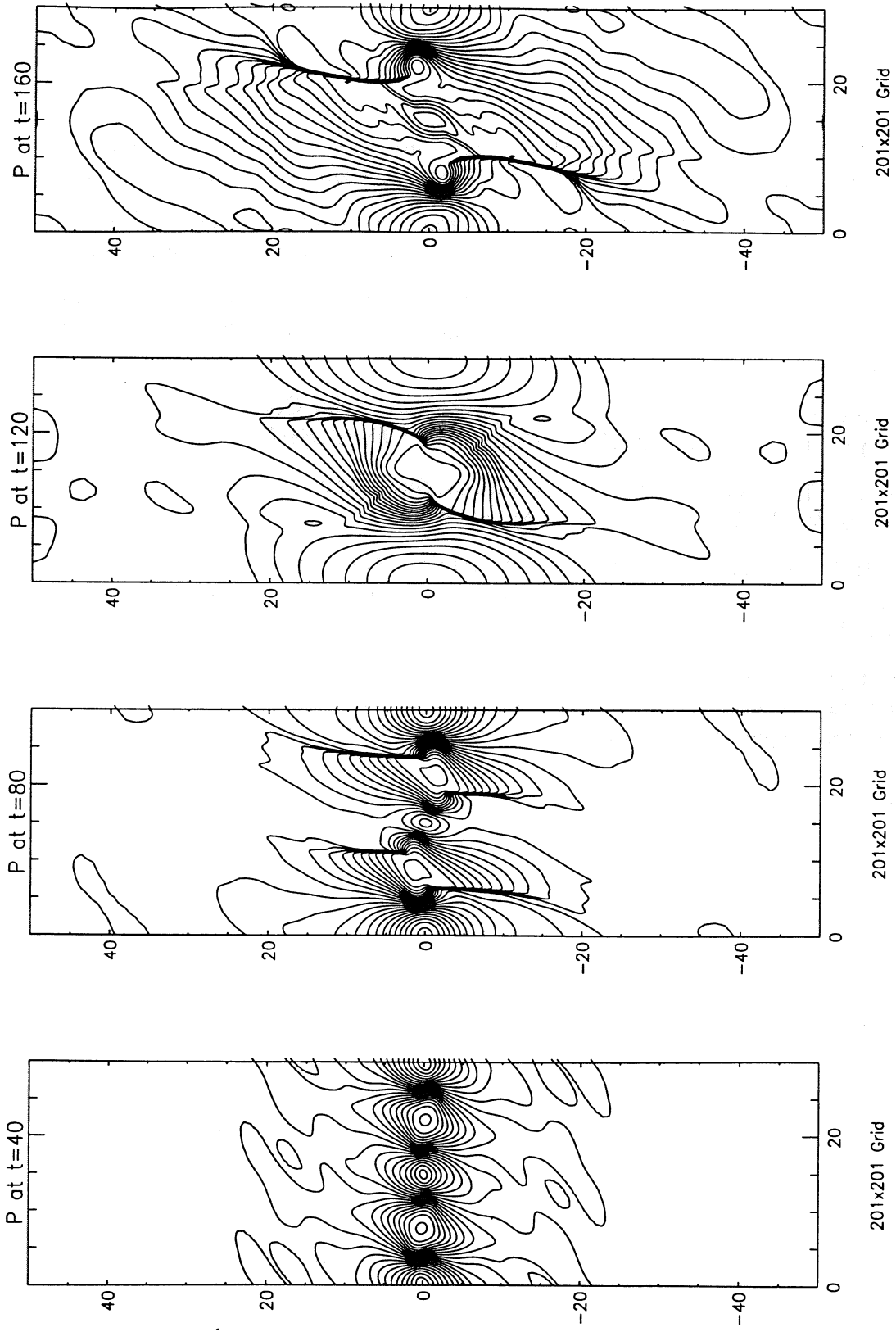
Figure 1. Four stages in the vortex pairing, at times $t = 40, 80, 120, 160$, showing (a) pressure, (b) density, (c) vorticity and (d) temperature contours for a $201 \times 201$ grid.

Figure 1. Cont. (Figure 1b)

ρ at t=160    ρ at t=120    ρ at t=80    ρ at t=40

201×201 Grid    201×201 Grid    201×201 Grid    201×201 Grid

21

Figure 1. Cont. (Figure 1c)

22

T at t=40

201×201 Grid

T at t=80

201×201 Grid

T at t=120

201×201 Grid

T at t=160
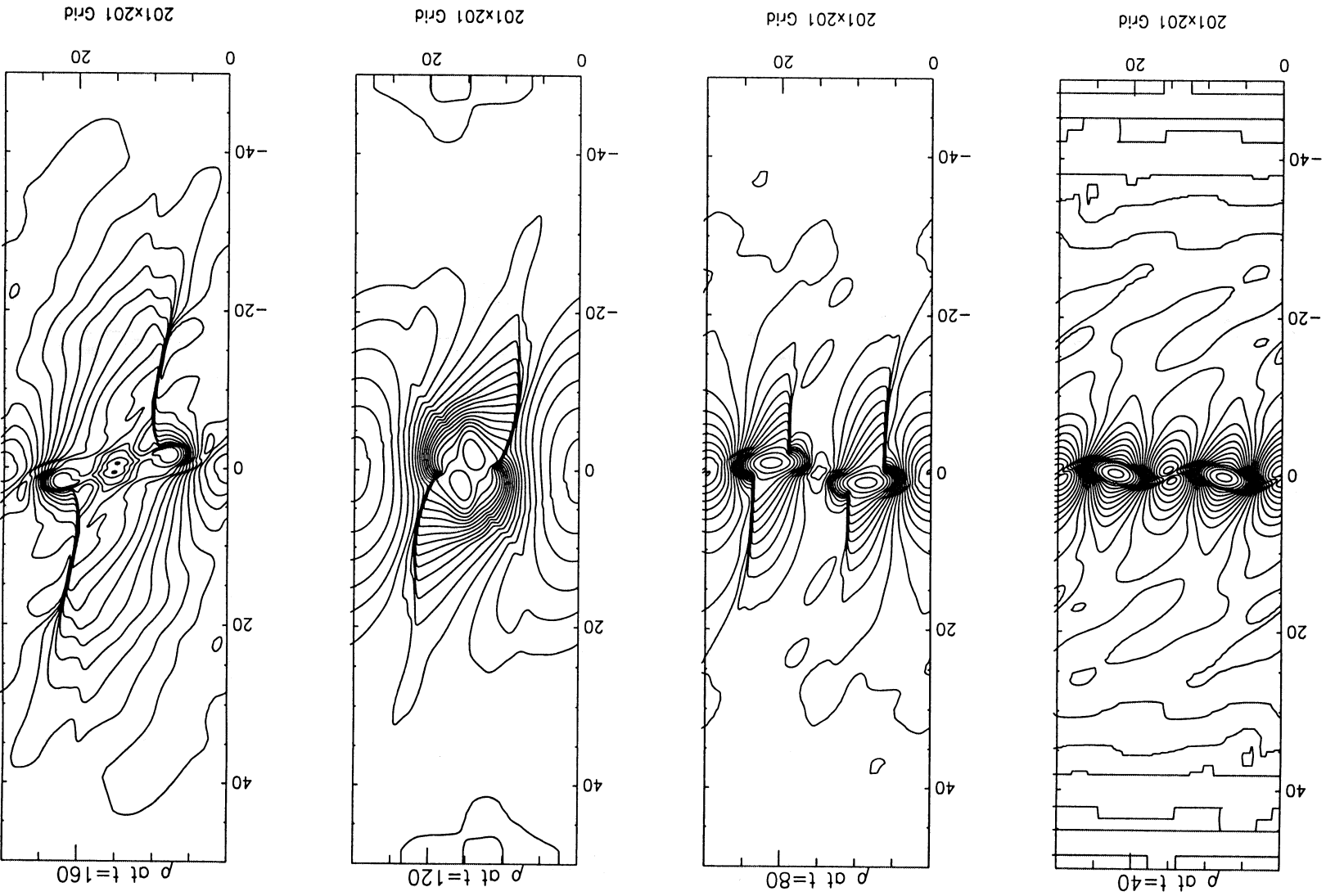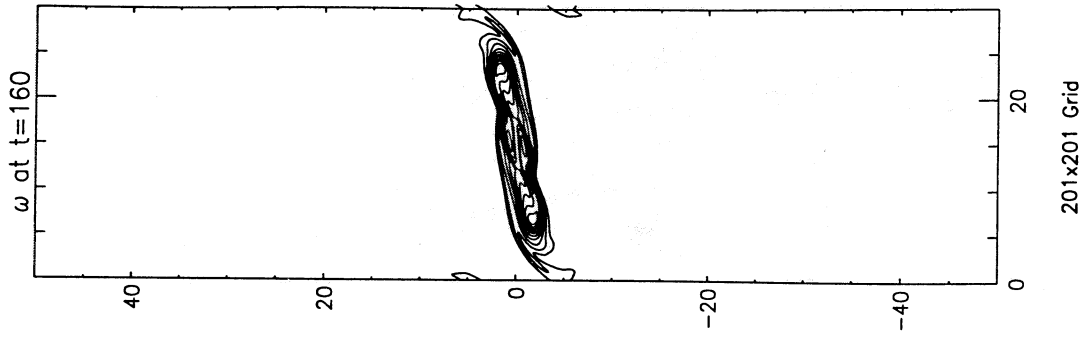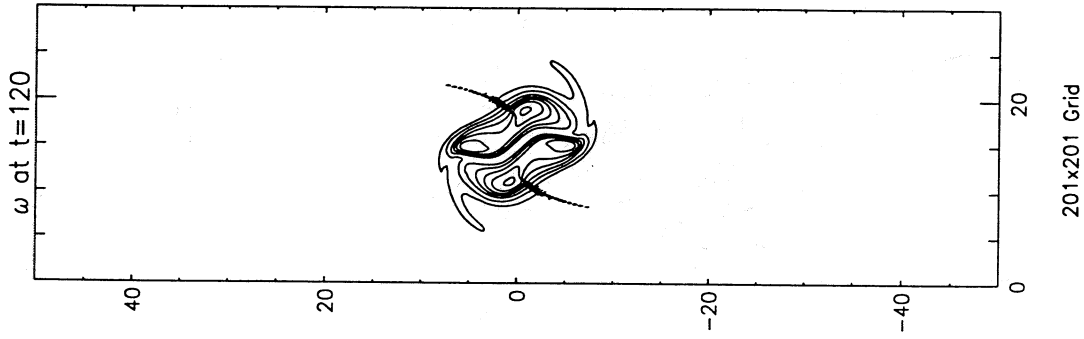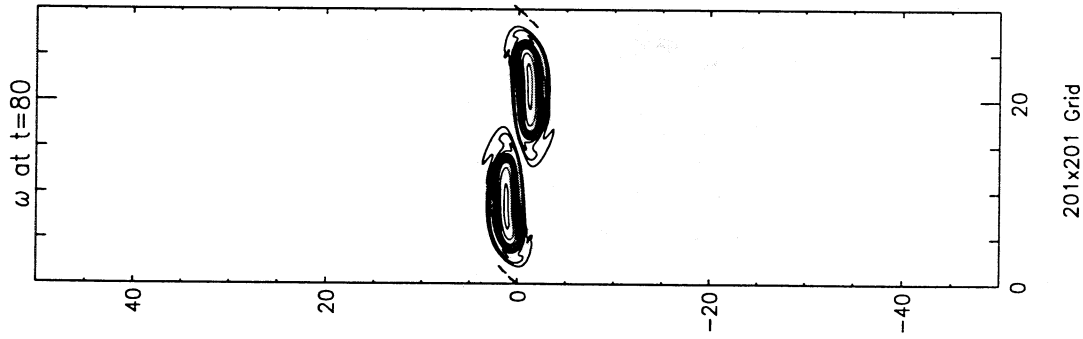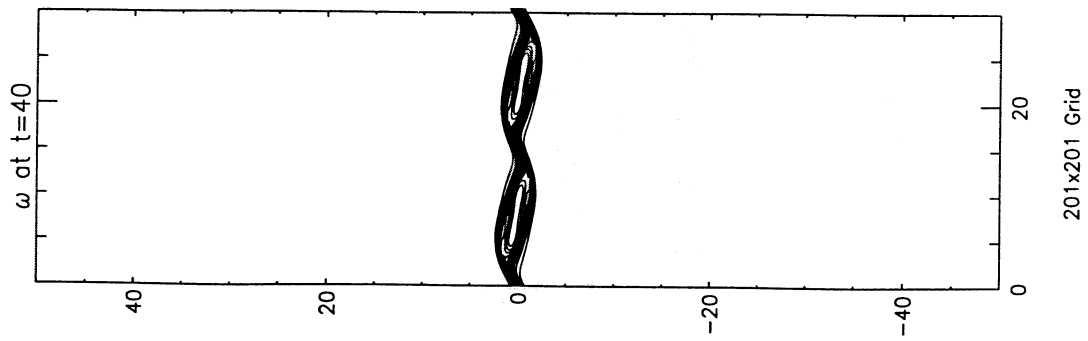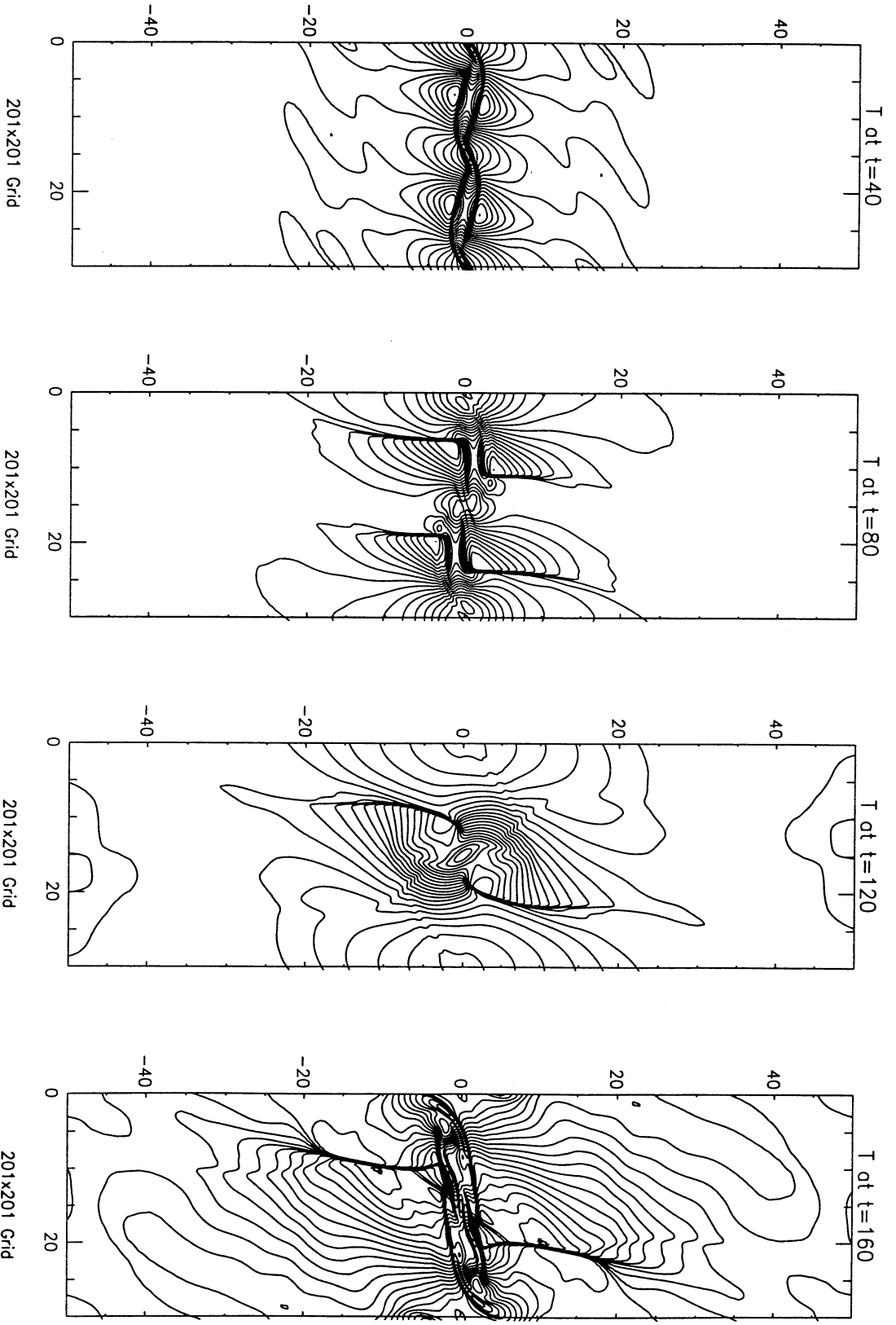
201×201 Grid

Figure 1. Cont. (Figure 1d)
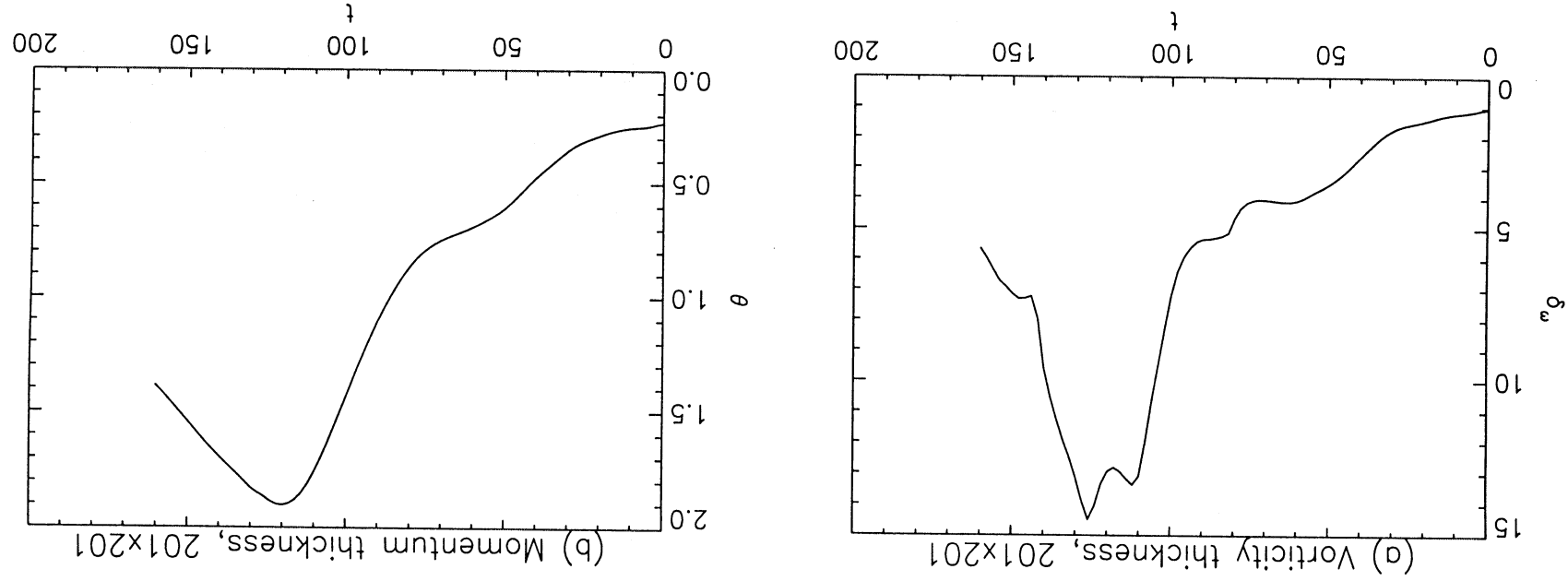
Figure 2. Growth of thickness of the time-developing mixing layer (a) vorticity thickness $\delta_\omega$ and (b) momentum thickness $\theta$ for a $201 \times 201$ grid.

(a) $\rho$ at t=120 (min= 0.358678 max= 2.38036), 321x81

(b) $p$ at t=120 (min= 0.325057 max= 0.552678), 321x81

(c) $T$ at t=120 (min= 0.201803 max= 1.06148), 321x81
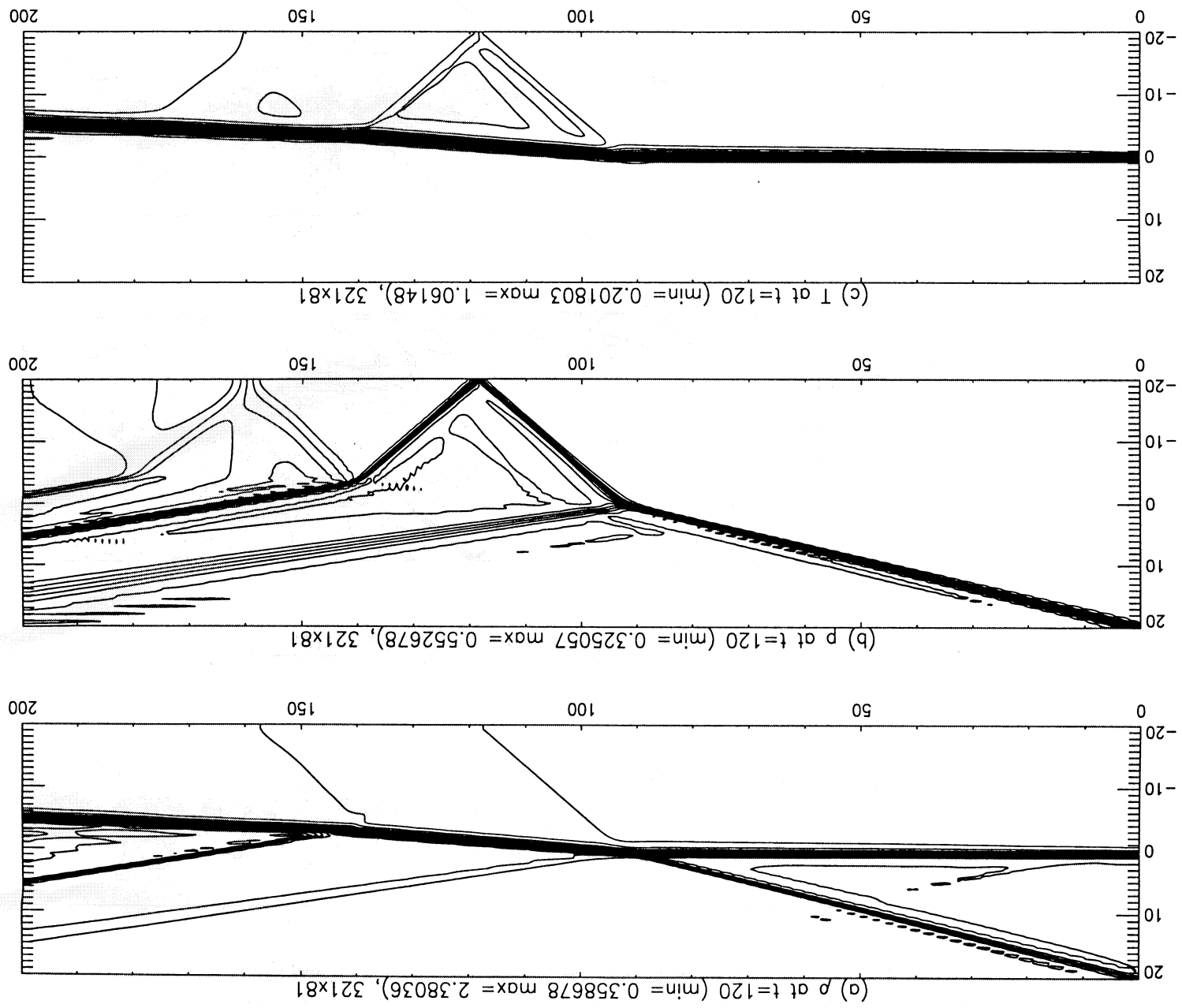
Figure 3. Structure of the laminar flow shock-shear-layer interaction problem at $t = 120$. Contours are shown of (a) pressure, (b) density and (c) temperature for a 321 × 81 grid.

25
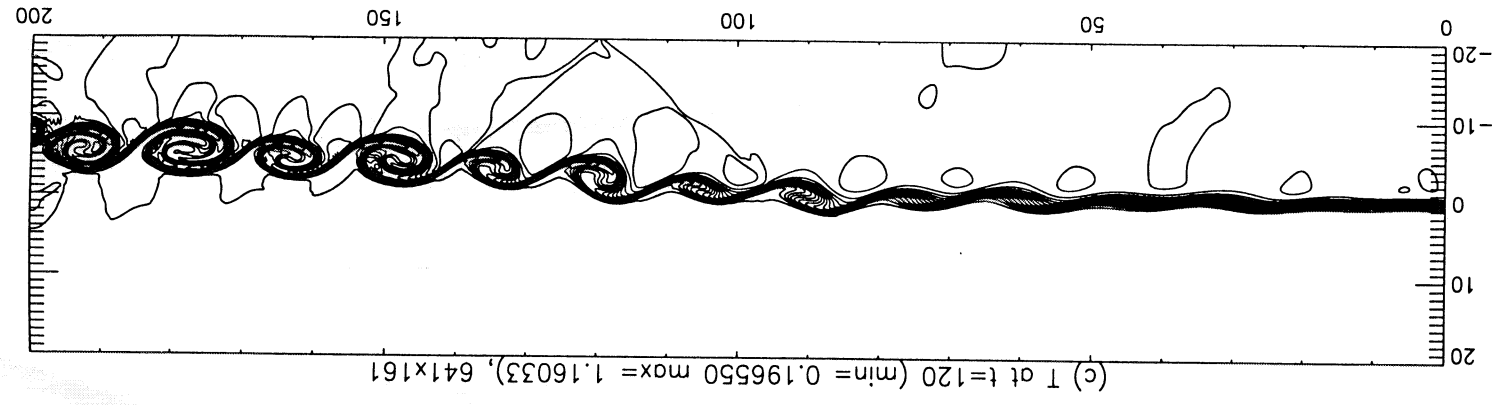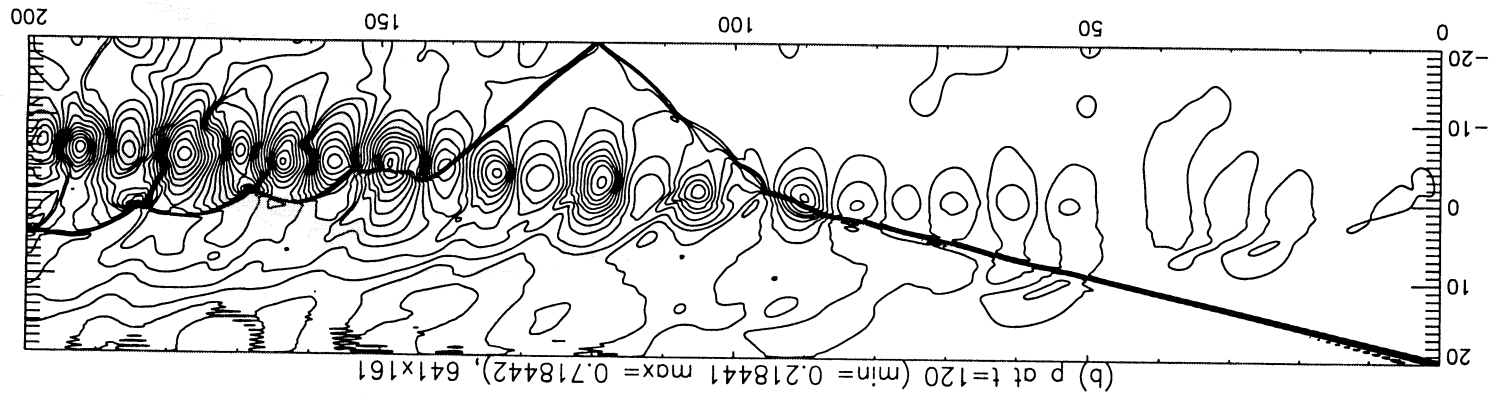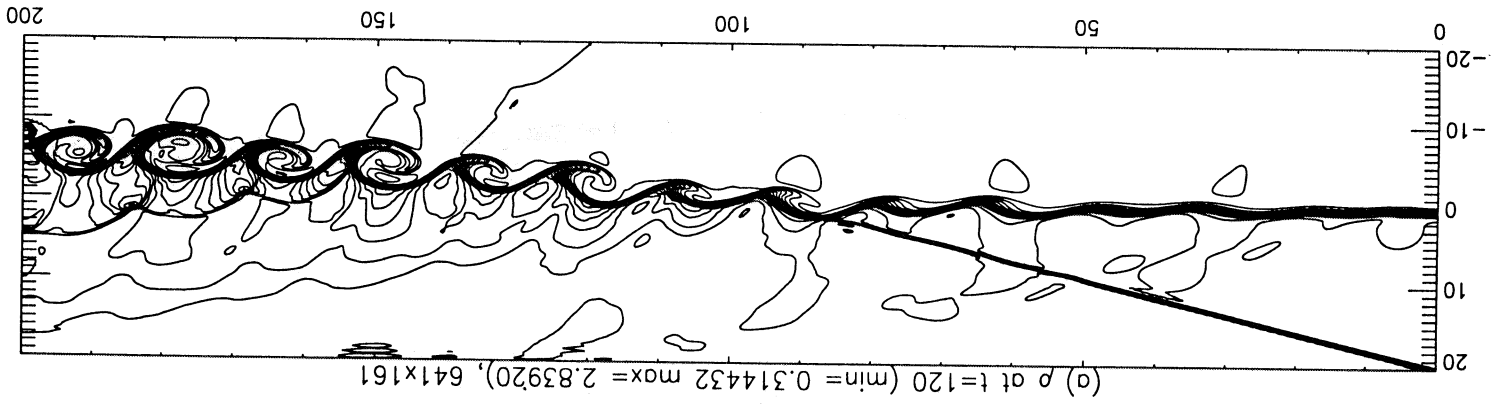
Figure 4. The reference solution for the shock-shear-layer interaction problem at $t = 120$. Contours are shown of (a) pressure, (b) density and (c) temperature for a $641 \times 161$ grid.

(c) $T$ at $t=120$ (min= 0.196550 max= 1.160033), 641×161

(b) $\rho$ at $t=120$ (min= 0.218441 max= 0.718442), 641×161

(a) $\rho$ at $t=120$ (min= 0.314432 max= 2.839320), 641×161

26

Figure 6. The effect of order of accuracy on the TVD methods, TVD22 (·····), TVD44 (- - -) and TVD66 (chain dotted), compared with the reference solution (solid line): (a) vorticity thickness $\delta_\omega$, (b) momentum thickness $\theta$ for a 101 × 101 grid.

## (a) Vorticity thickness, 101x101

## (b) Momentum thickness, 101x101
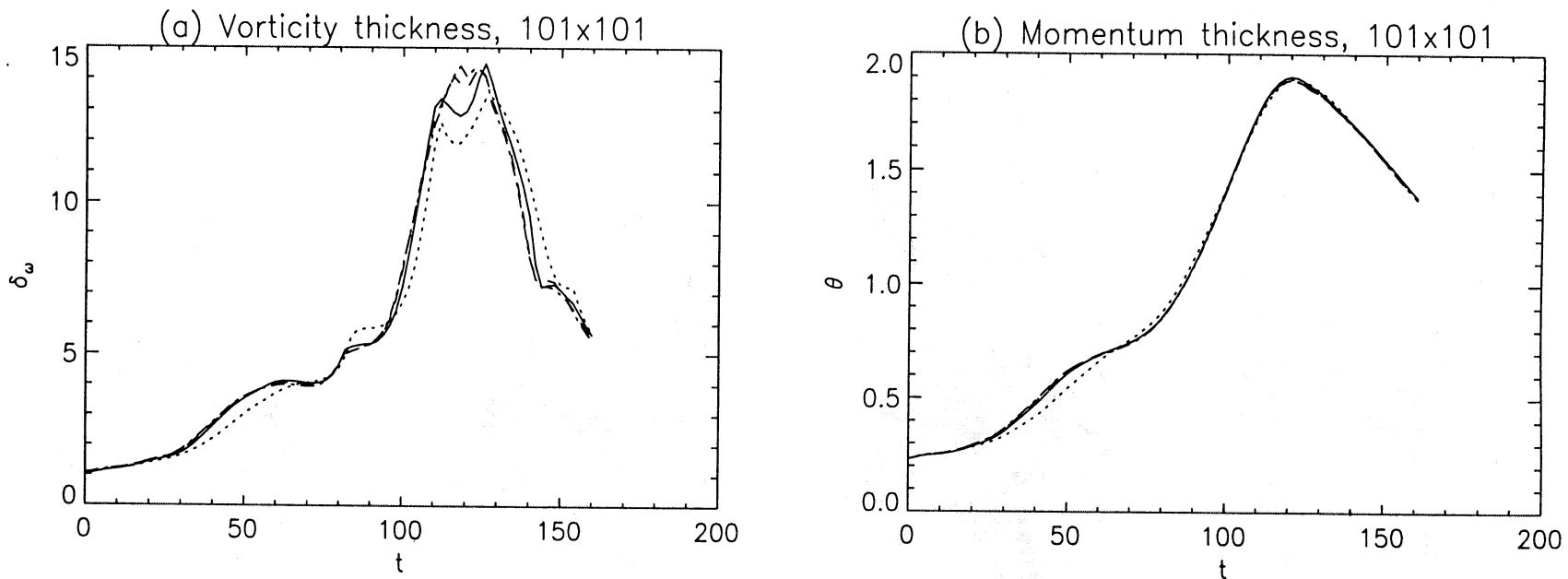
Figure 7. The effect of order of accuracy on the ACM methods, ACM22 (....), ACM44 (- - -) and ACM66 (chain dotted), compared with the reference solution (solid line): (a) vorticity thickness $\delta_\omega$, (b) momentum thickness $\theta$ for a $101 \times 101$ grid.
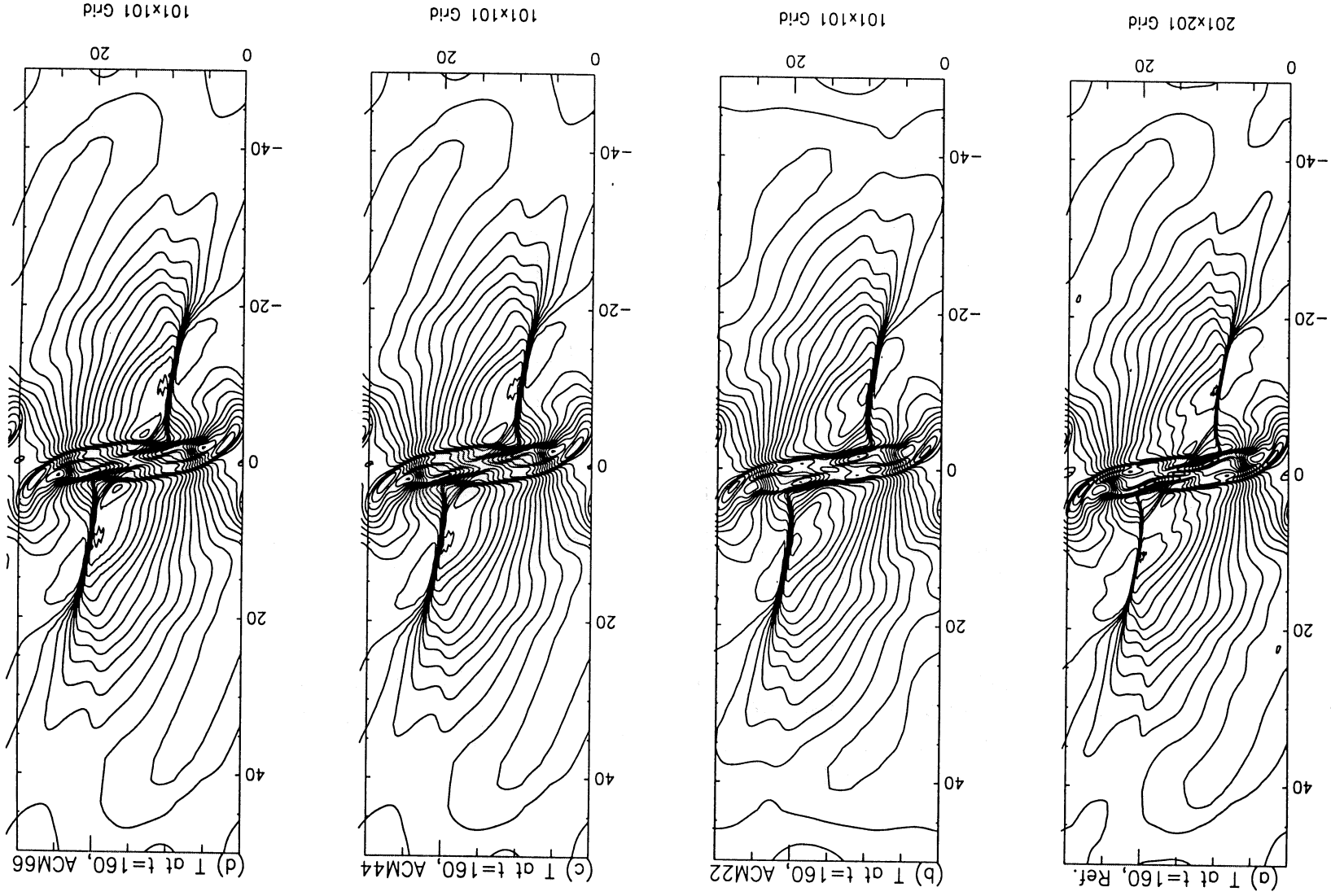
Figure 8. Comparative shock resolution properties of schemes of different order, illustrated by temperature contours at $t = 160$: (a) reference solution, (b) ACM22, (c) ACM44, and (d) ACM66 for a $101 \times 101$ grid.

30
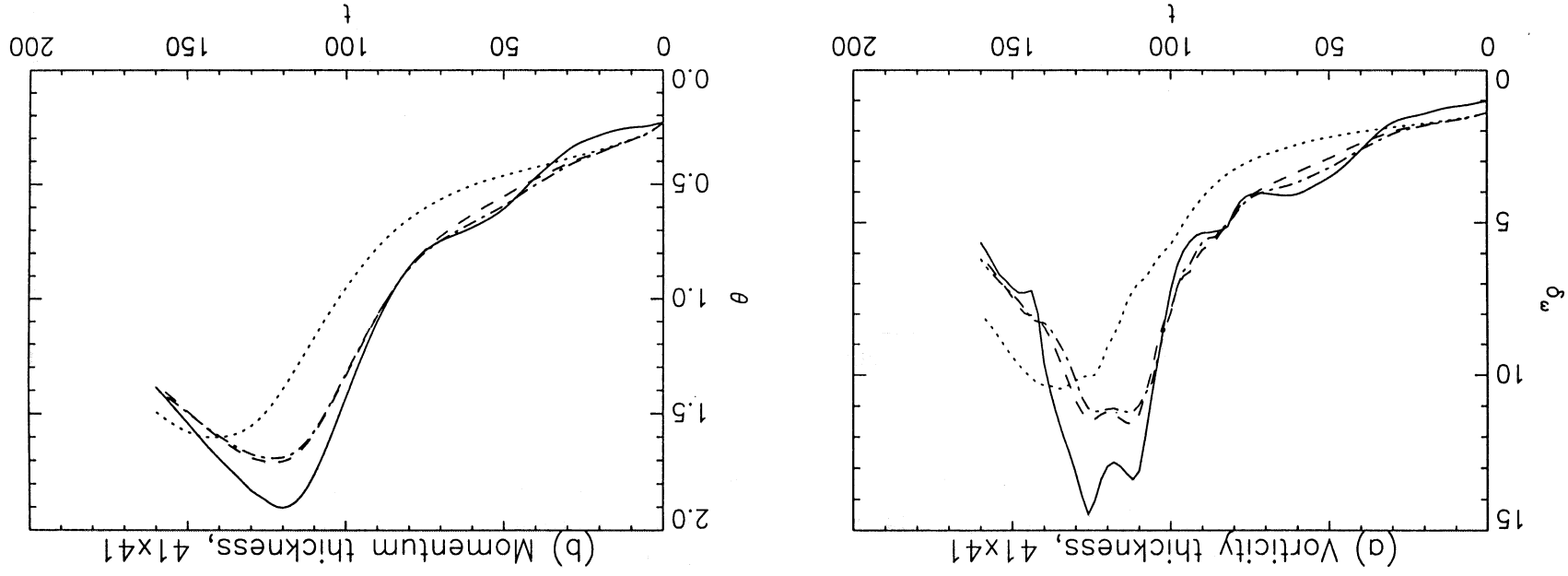
Figure 9. The effect of order of accuracy on the ACM methods at very coarse grid (41 × 41): ACM22 (····), ACM44 (- - -) and ACM66 (chain dotted), compared with the reference solution (solid line): (a) vorticity thickness $\delta_\omega$, (b) momentum thickness $\theta$.

(a) Vorticity thickness, 41×41

(b) Momentum thickness, 41×41
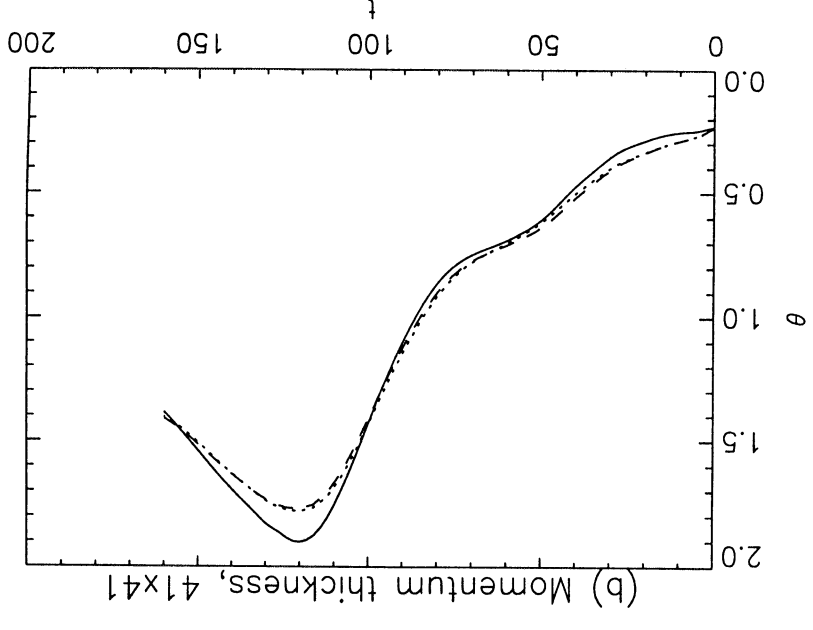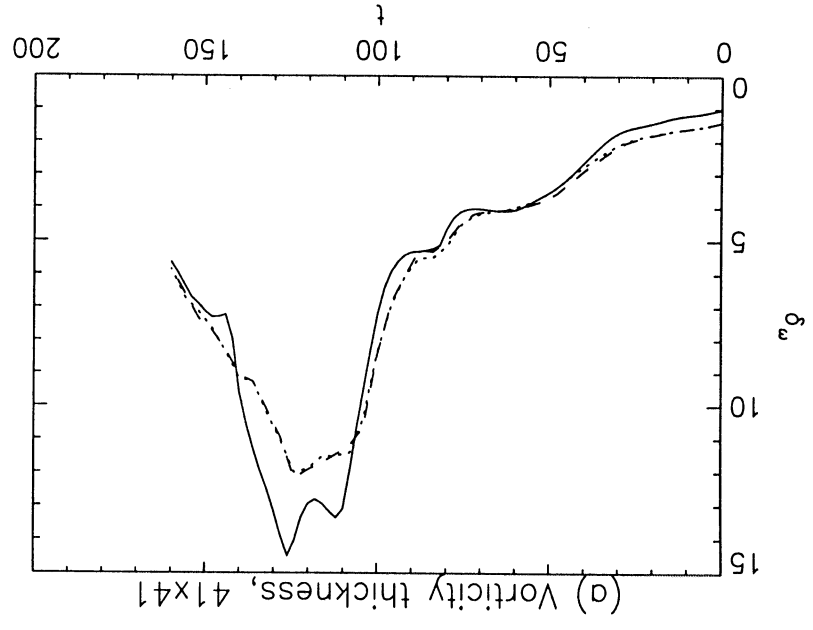
Figure 10. Compact schemes applied at very coarse grid (41 × 41): ACM44C (·····), ACM66C (– – –) compared with the reference solution (solid line): (a) vorticity thickness $\delta_w$, (b) momentum thickness $\theta$.
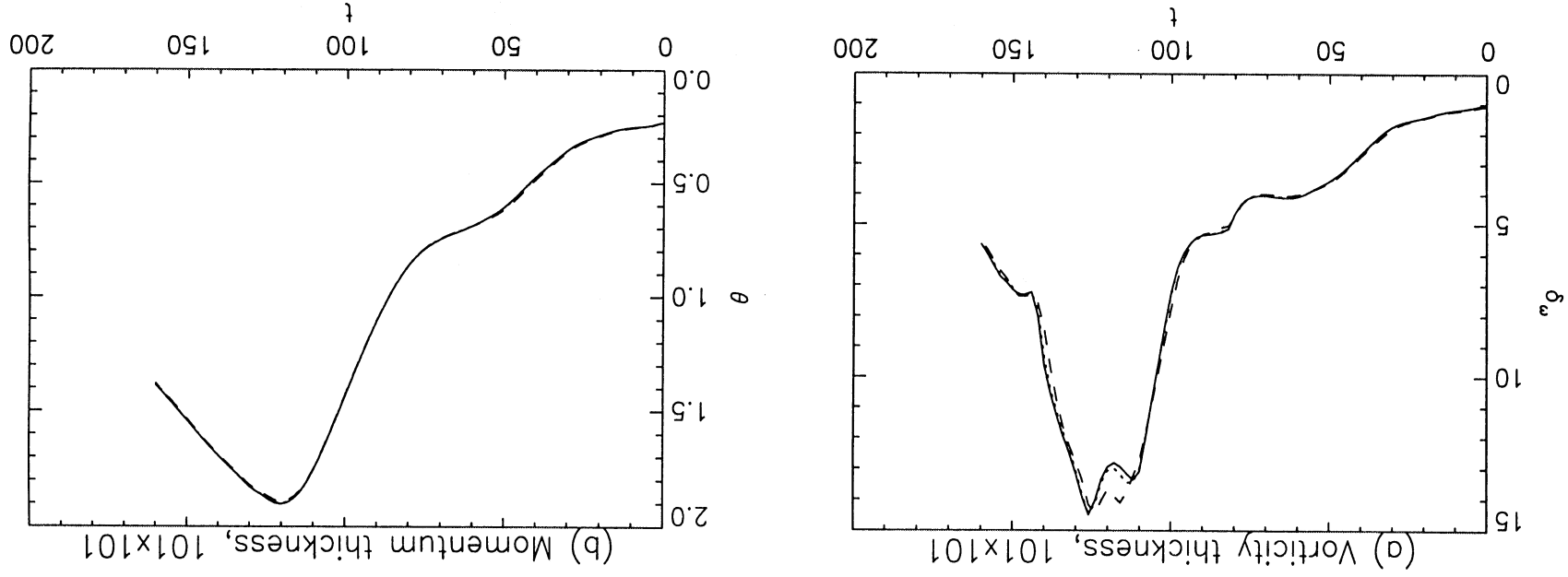
Figure 11. Comparison of the reference solution (solid line) with the same grid and scheme ACM44 but using $\kappa = 0.7$ for all fields (·····) and ACM44 using $\kappa = 0.35$ for all fields for a $101 \times 101$ grid (- - -): (a) vorticity thickness $\delta_\omega$, (b) momentum thickness $\theta$.
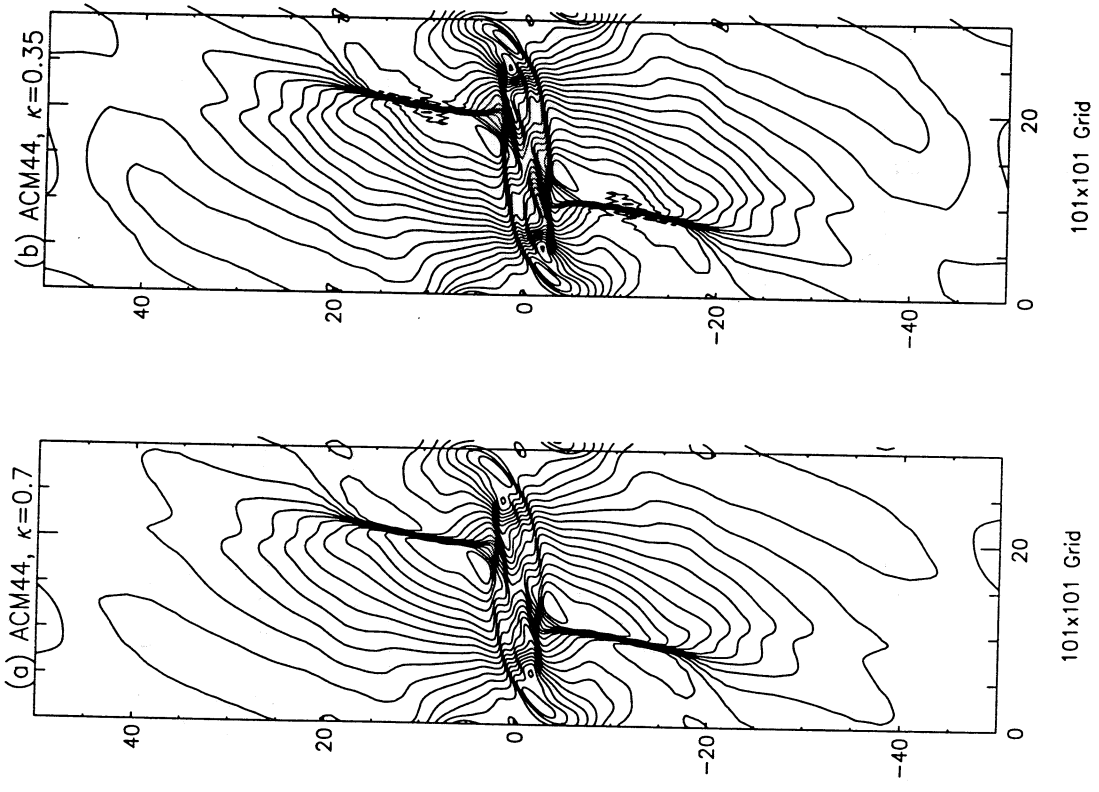
Figure 12. Comparison of the temperature contours at $t = 160$ for ACM44: (a) $\kappa = 0.7$ for all fields and (b) $\kappa = 0.35$ for all fields for a $101 \times 101$ grid.

34
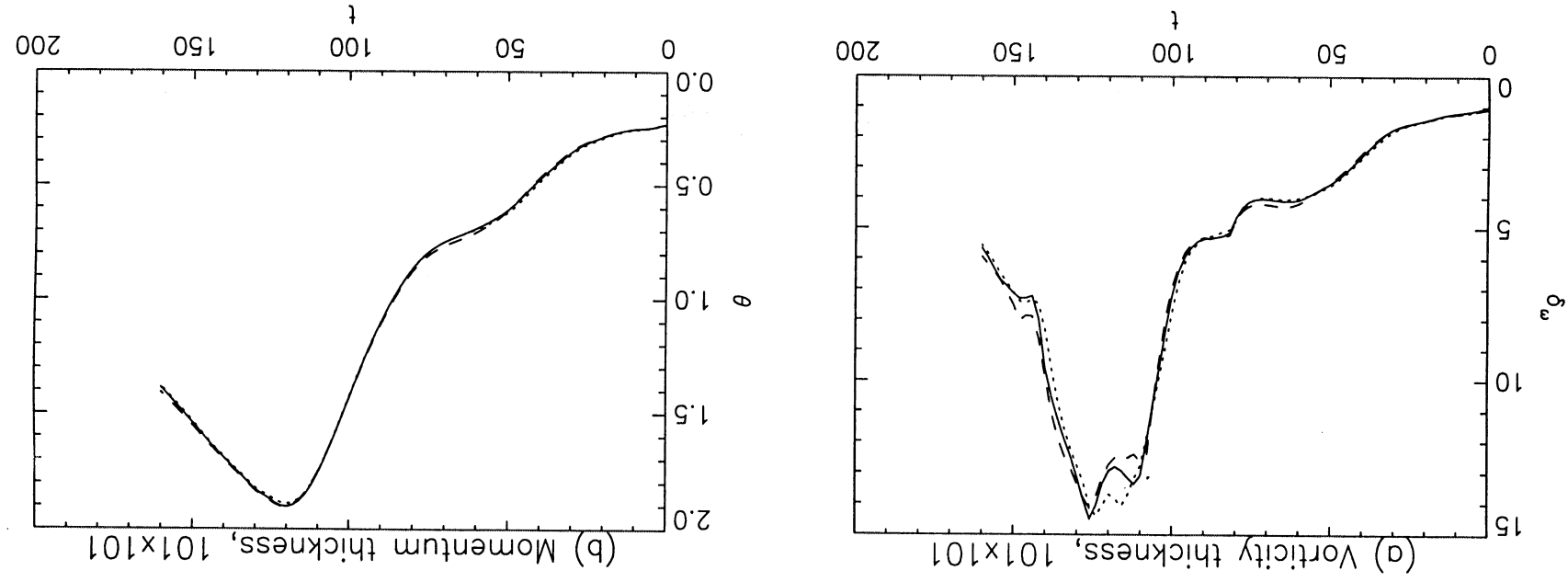
Figure 13. Comparison of the reference solution (solid line) with the ACM44,
$\kappa = 0.35$ for all fields (....) and ACM44 using $\kappa = 0.7$ for the nonlinear fields
and $\kappa = 0$ for the linear fields for a $101 \times 101$ grid (- - -): (a) vorticity
thickness $\delta_\omega$, (b) momentum thickness $\theta$.

(a) Vorticity thickness, 101×101

(b) Momentum thickness, 101×101
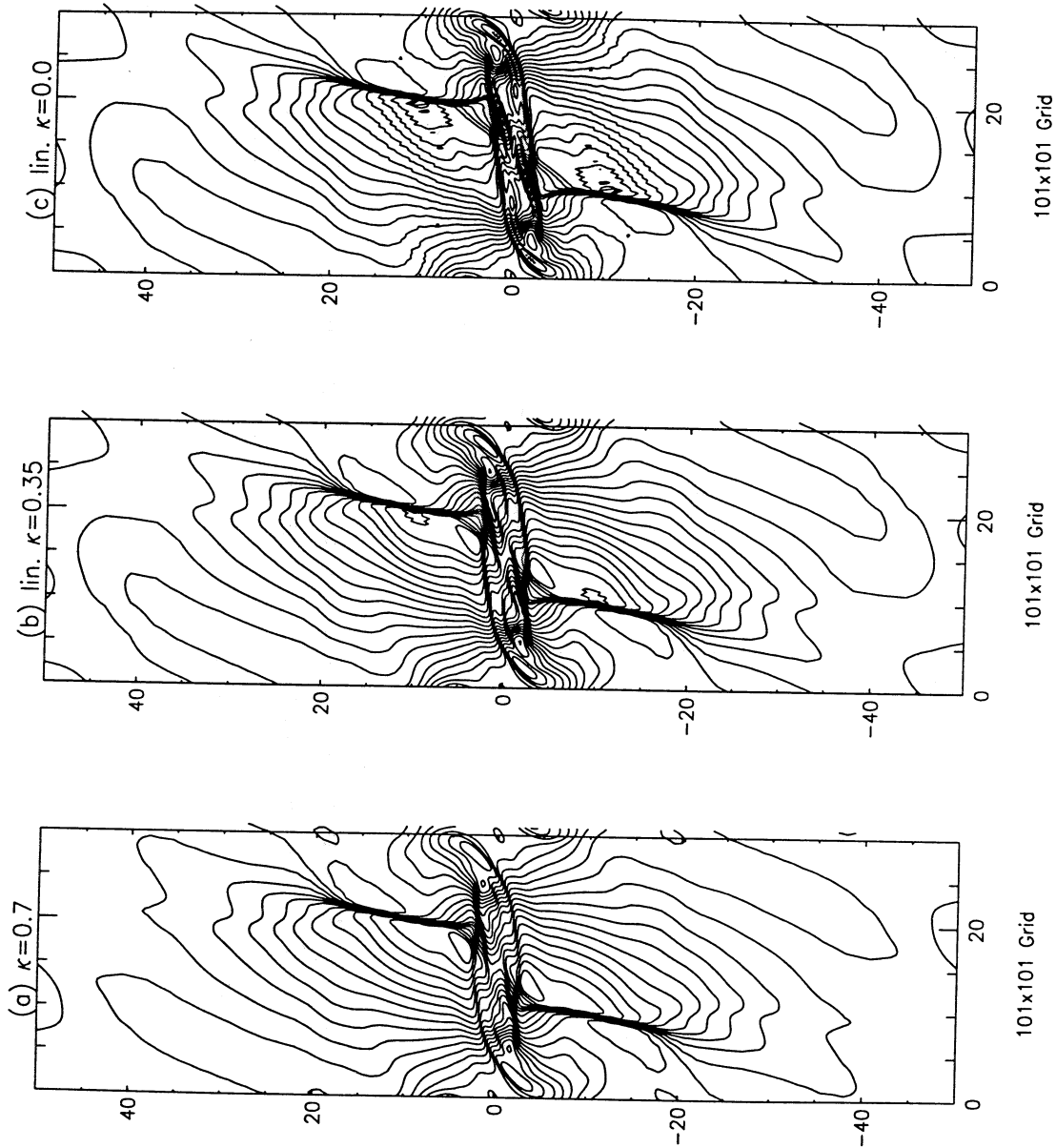
Figure 14. Effect of $\kappa$ in the ACM44 scheme on the fine scale flow structure, illustrated by temperature contours at $t = 160$: (a) $\kappa = 0.7$ for all fields, (b) $\kappa = 0.7$ for the nonlinear fields and $\kappa = 0.35$ for the linear fields and (c) $\kappa = 0.7$ for the nonlinear fields and $\kappa = 0.0$ for the linear fields for a $101 \times 101$ grid.
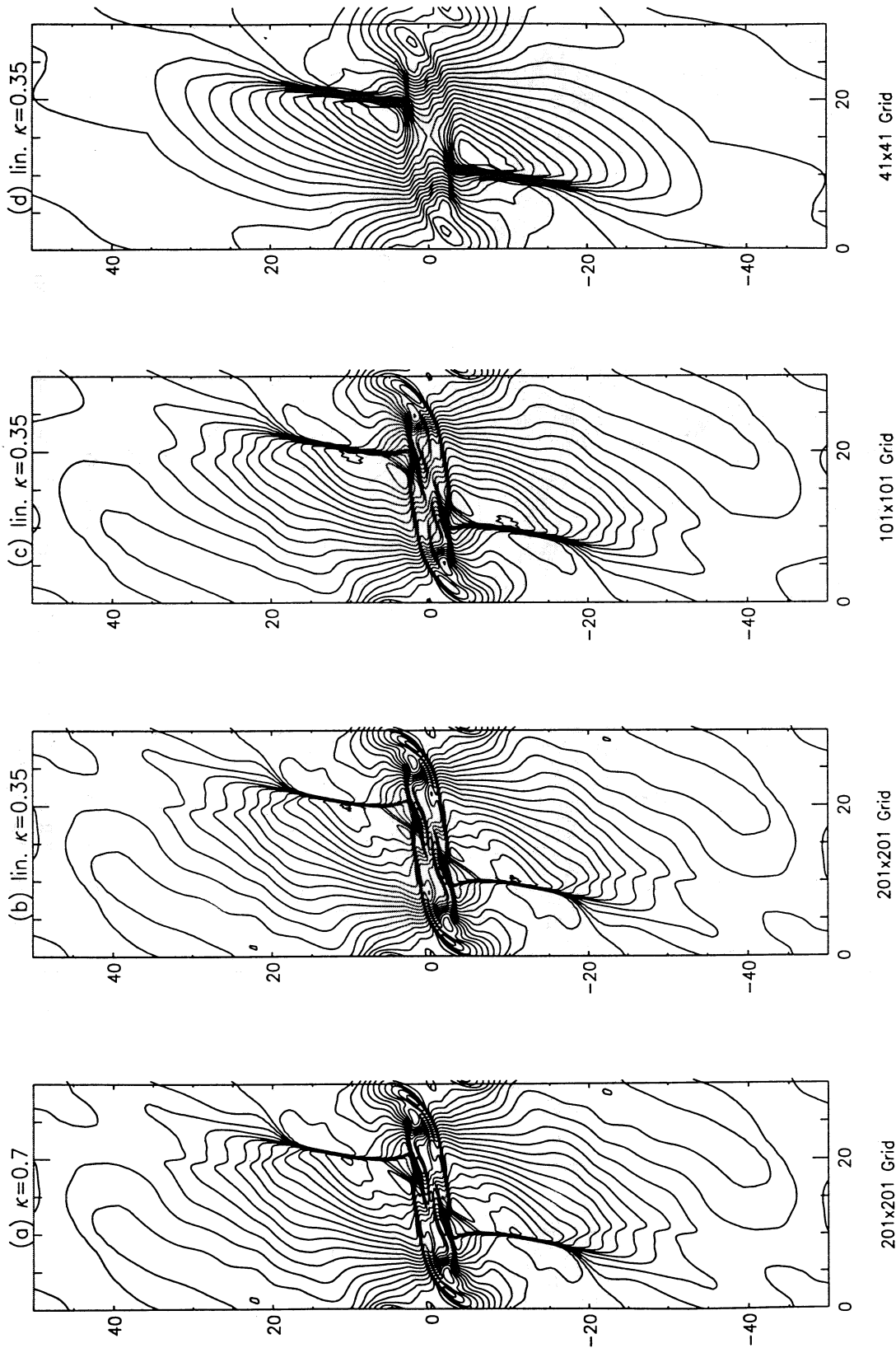
Figure 15. Effect of $\kappa$ constant in the ACM44 scheme on the fine scale flow structure, illustrated by temperature contours at $t = 160$ for three different grids: (a) $\kappa = 0.7$ for all fields ($201 \times 201$), (b) $\kappa = 0.7$ for the nonlinear fields and $\kappa = 0.35$ for the linear fields ($201 \times 201$), (c) $\kappa = 0.7$ for the nonlinear fields and $\kappa = 0.35$ for the linear fields ($101 \times 101$), and (d) $\kappa = 0.7$ for the nonlinear fields and $\kappa = 0.35$ for the linear fields ($41 \times 41$),
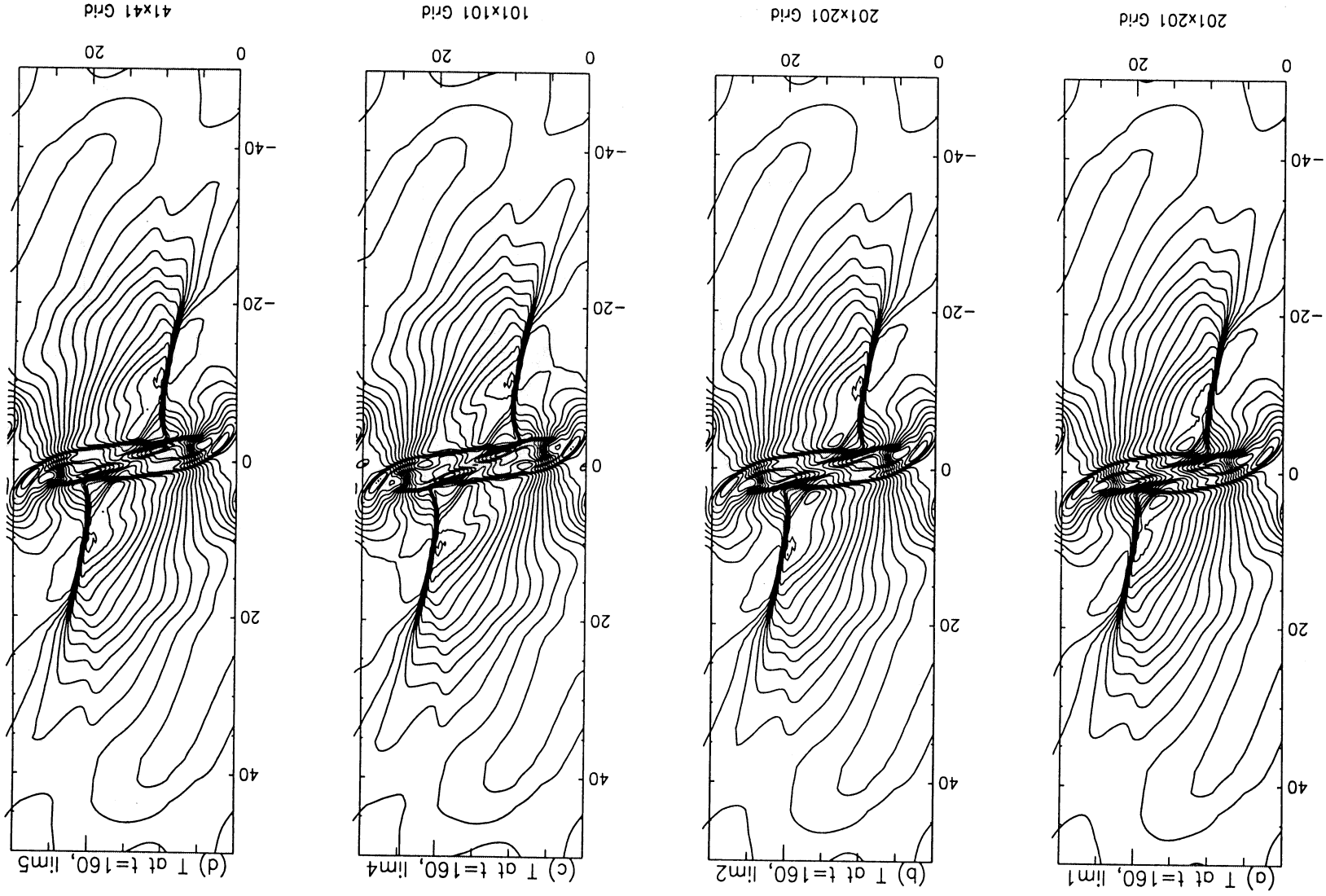
37
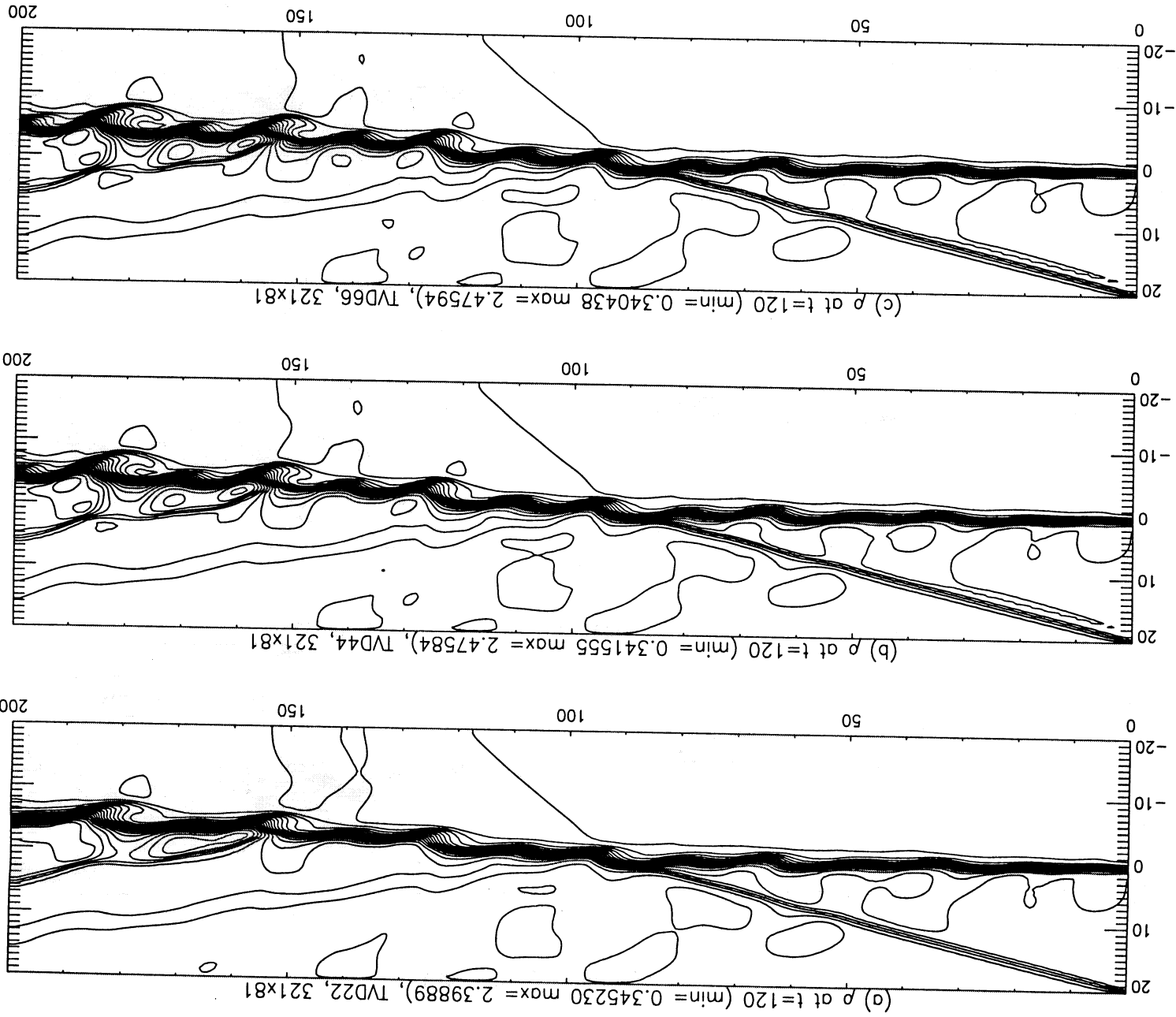
Figure 17. Comparison of density contours at $t = 120$ for the shock-shear-layer test case: (a) TVD22, TVD44 and TVD66, (b) ACM22, ACM44 and ACM66 and (c) reference solution ($641 \times 161$), TVD44 and ACM44 for a $321 \times 81$ grid.

(c) $\rho$ at $t=120$ (min= 0.340438 max= 2.47594), TVD66, 321×81

(b) $\rho$ at $t=120$ (min= 0.341555 max= 2.47584), TVD44, 321×81

(a) $\rho$ at $t=120$ (min= 0.345230 max= 2.39989), TVD22, 321×81
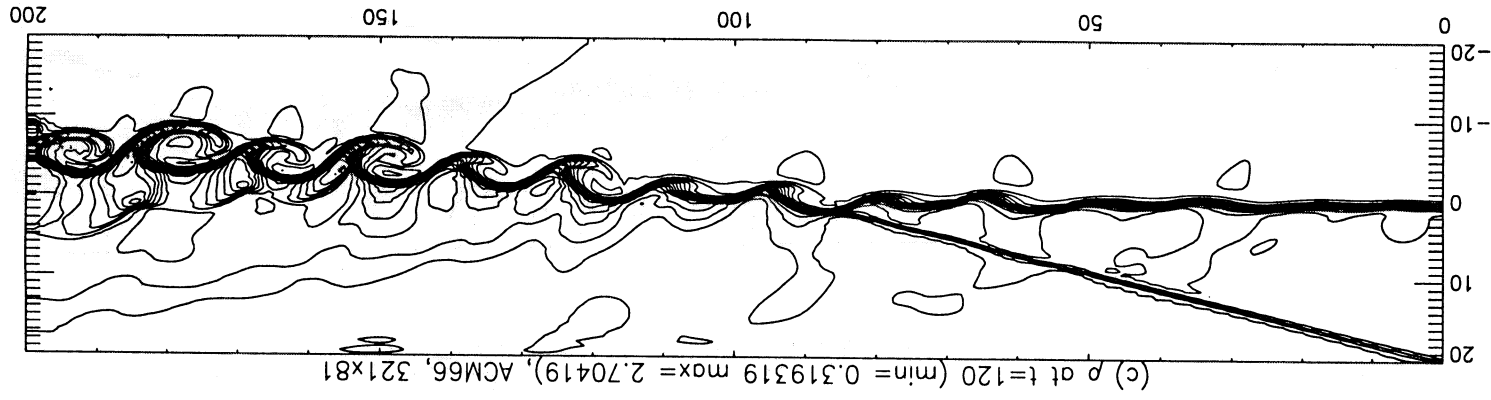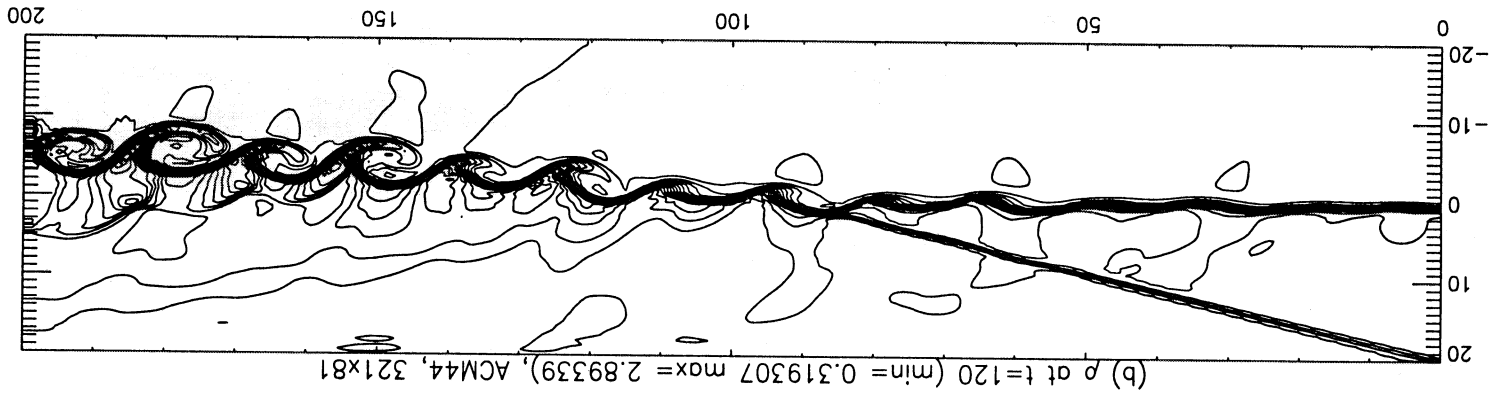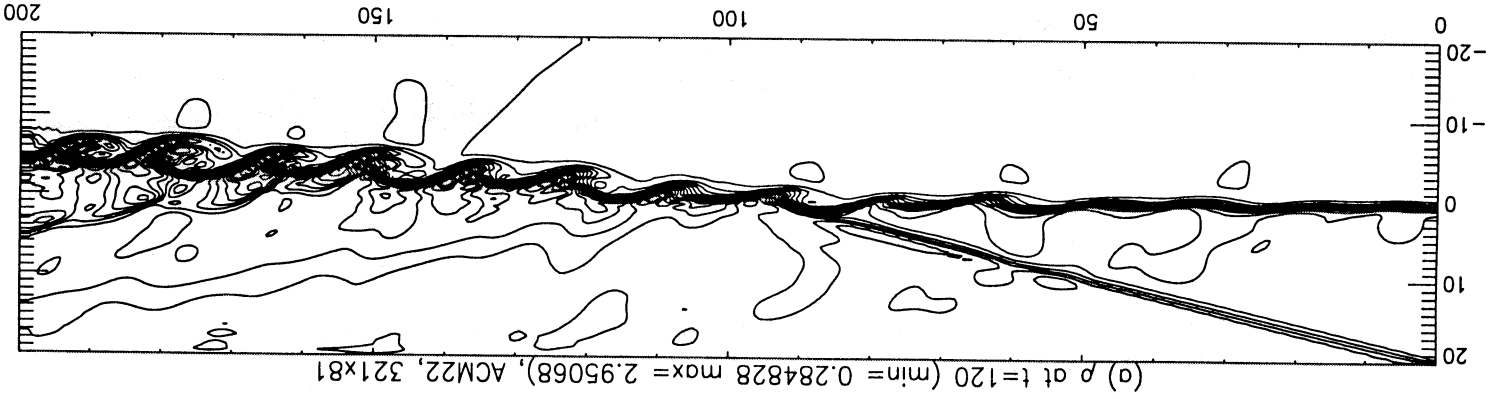
Figure 17. Cont. (Figure 17c)

41
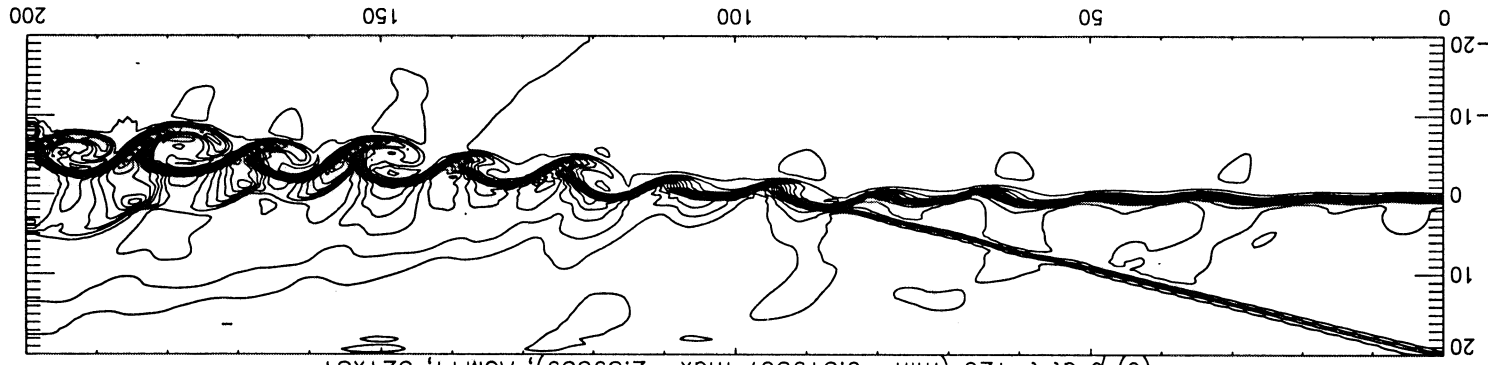
(c) $\rho$ at t=120 (min=0.319307 max=2.89339), ACM44, 321x81
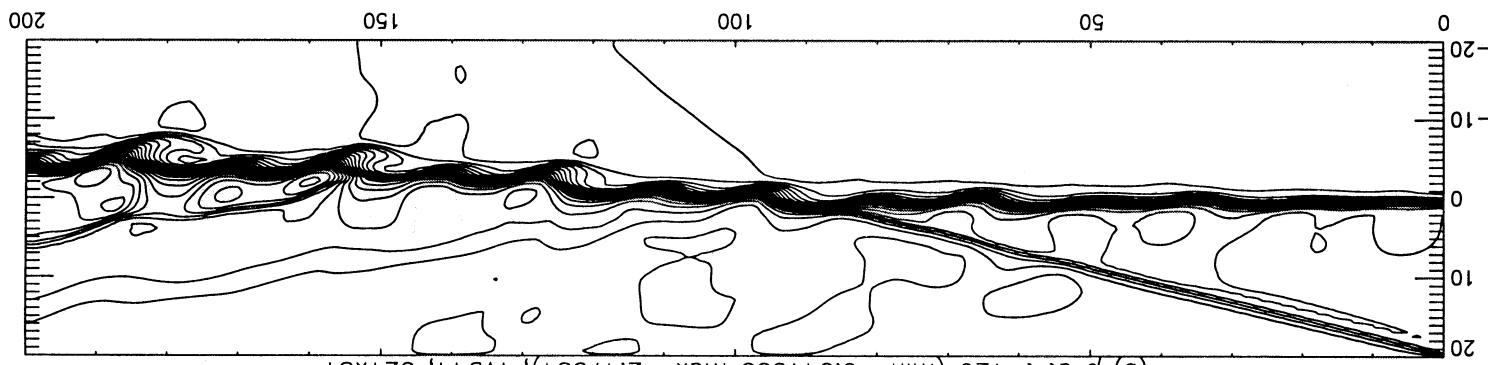
(b) $\rho$ at t=120 (min=0.341555 max=2.47584), TVD44, 321x81
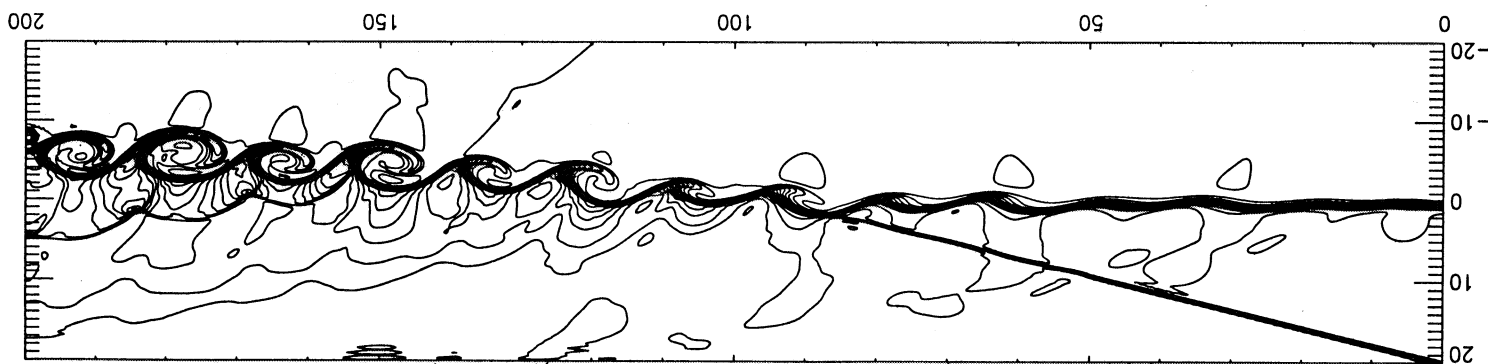
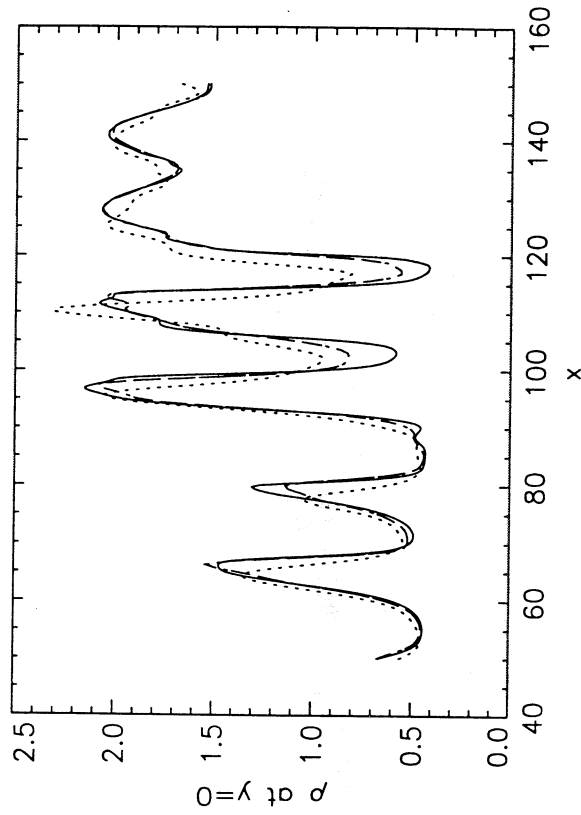(a) $\rho$ at t=120 (min=0.314432 max=2.83920), ACM44, 641x161

Figure 19. Slice through the density field showing the effect of order of accuracy on the ACM methods: ACM22 (....), ACM44 (- - -) and ACM66 (chain dotted) for a 321×81 grid, compared with the reference solution (solid line).
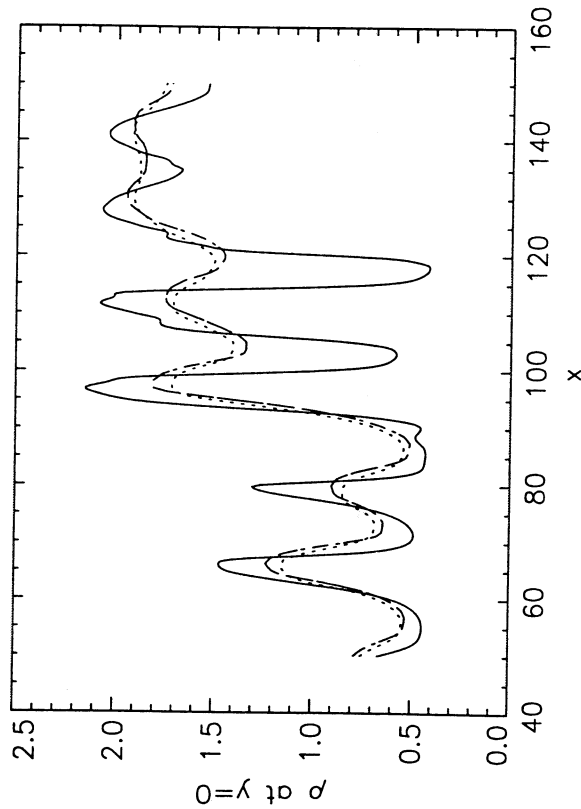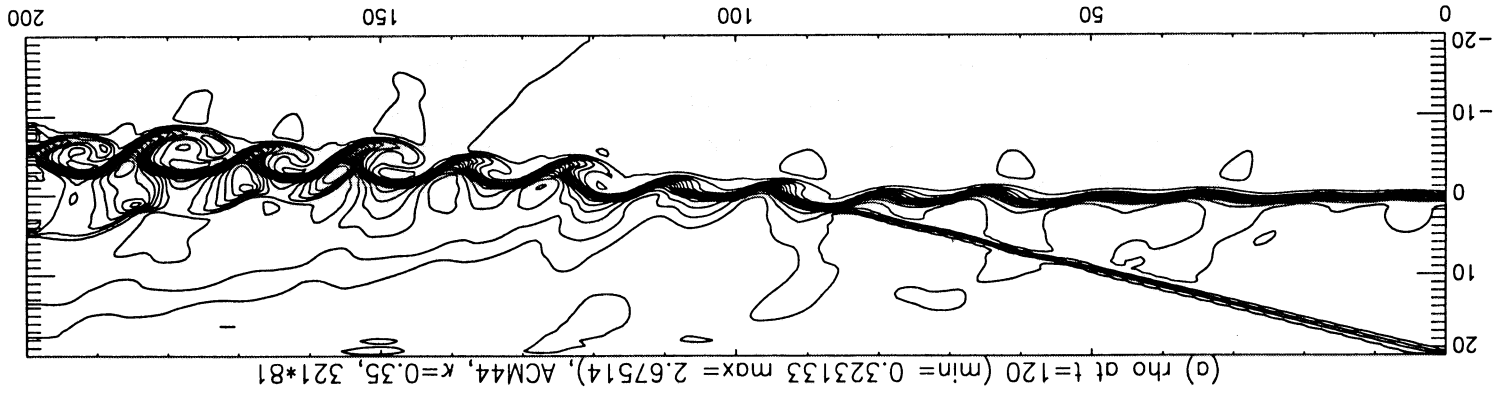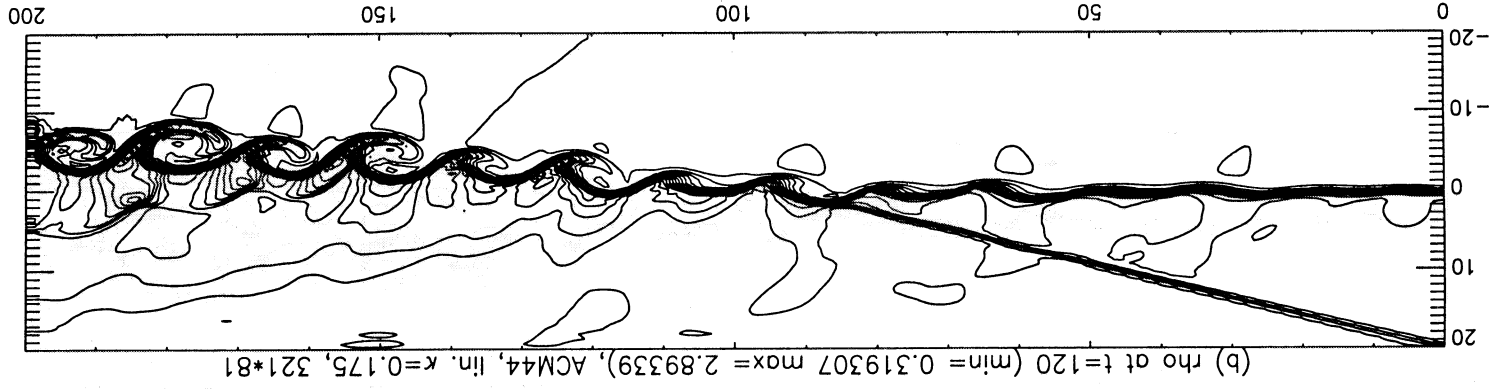
Figure 18. Slice through the density field showing the effect of order of accuracy on the TVD methods: TVD22 (....), TVD44 (- - -) and TVD66 (chain dotted) for a 321 × 81 grid, compared with the reference solution (solid line).

Figure 20.  Comparison of density contours at $t = 120$ for the shock-shear-layer test case: (a) ACM44, $\kappa = 0.35$ for all fields, and (b) ACM44, $\kappa = 0.35$ for the nonlinear fields and $\kappa = 0.175$ for the linear fields for a $321 \times 81$ grid.
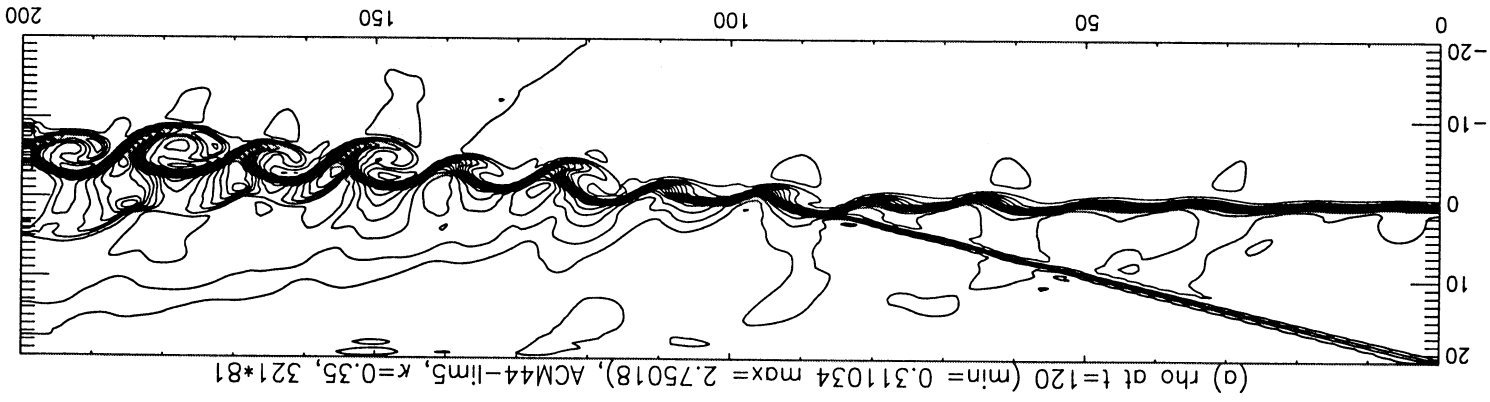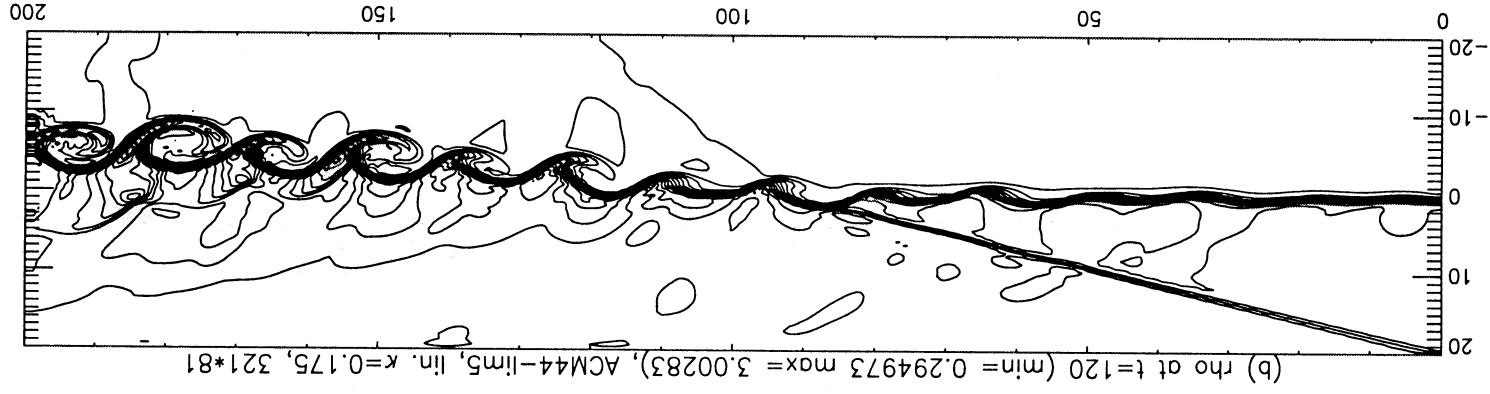


(b) rho at t=120 (min= 0.319307 max= 2.89339), ACM44, lin. $\kappa$=0.175, 321*81

(a) rho at t=120 (min= 0.323133 max= 2.67514), ACM44, $\kappa$=0.35, 321*81